



Soberano, O. B., Gabo-Ratio, J. A. S., Queaño, K. L., Dimalanta, C. B., Yumul Jr., G. P., Andal, E. S., Yonezu, K. and Boyce, A. J. (2021) Mineral chemistry, fluid inclusion and stable isotope studies of the Suyoc epithermal veins: insights to Au-Cu mineralization in southern Mankayan Mineral District, Philippines. *Ore Geology Reviews*, 131, 104035. (doi: [10.1016/j.oregeorev.2021.104035](https://doi.org/10.1016/j.oregeorev.2021.104035)).

This is the author's final accepted version.

There may be differences between this version and the published version. You are advised to consult the publisher's version if you wish to cite from it.

<http://eprints.gla.ac.uk/233883/>

Deposited on: 10 February 2021

Enlighten – Research publications by members of the University of Glasgow
<http://eprints.gla.ac.uk>

1 Mineral chemistry, fluid inclusion and stable isotope studies of the Suyoc epithermal
2 veins: Insights to Au-Cu mineralization in southern Mankayan Mineral District,
3 Philippines

4
5 O.B. Soberano¹, J.A.S. Gabo-Ratio¹, K.L. Queaño², C.B. Dimalanta¹,
6 G.P. Yumul, Jr.³, E.S. Andal⁴, K. Yonezu⁵ and A.J. Boyce⁶

7 ¹Rushurgent Working Group, National Institute of Geological Sciences, College of
8 Science, University of the Philippines, Diliman, Quezon City 1101, Philippines

9 ²Department of Environmental Science, School of Science and Engineering,
10 Ateneo de Manila University, Loyola Heights, Quezon City 1108, Philippines

11 ³Cordillera Exploration Company Incorporated, Bonifacio Global City, Taguig City
12 1634, Philippines

13 ⁴Itoyon-Suyoc Resources Incorporated, Suyoc, Mankayan, Benguet 2608, Philippines

14 ⁵Department of Earth Resources Engineering, Faculty of Engineering, Kyushu
15 University, Fukuoka 819-0395, Japan

16 ⁶Scottish Universities Environmental Research Centre, Glasgow G75 0QF, United
17 Kingdom

18

19 **Abstract**

20 The Suyoc prospect is an epithermal vein-type mineralization located at the
21 southern part of the Mankayan Mineral District, Northern Luzon, Philippines. The
22 prospect's epithermal veins are hosted in volcanoclastic rocks and conglomerate, which
23 belong to the Late Oligocene to Early Miocene Balili Formation and the Middle to Late
24 Miocene Suyoc Conglomerate, respectively. These veins are classified into three major
25 types: quartz vein, quartz-sulfide vein, and quartz-carbonate vein. The quartz vein
26 exhibits massive and cockade textures associated with pyrite + chalcopyrite. The
27 quartz-sulfide vein consists of massive and comb quartz associated with pyrite +
28 chalcopyrite + sphalerite. The quartz-carbonate vein has massive quartz associated with

29 rhodochrosite and chalcopyrite + sphalerite + galena + Au/Ag ± bournonite. In addition,
30 massive gypsum ± pyrite occurs as a minor vein-type.

31 Fluid inclusion measurements in quartz from the three major vein-types
32 revealed 230-250°C formation temperatures and 1.0-3.5 wt.% NaCl equivalent salinity,
33 which are values consistent with epithermal deposits. Quartz textures (e.g., massive,
34 cockade, comb, crustiform) and dominance of liquid-rich fluid inclusions do not
35 suggest that boiling is a primary mechanism of vein deposition. Possible mechanisms
36 are inferred as meteoric water dilution based on homogenization versus salinity trend
37 in quartz vein and presence of rhodochrosite in quartz-carbonate vein, and wall rock
38 interaction based on FeS trend in sphalerite crystals of the quartz-carbonate vein. The
39 presence of pyrite and chalcopyrite in the major vein-types and the FeS mole percent
40 values (0.51 to 8.30) in quartz-carbonate vein indicate an intermediate sulfidation state.
41 The alteration minerals illite chlorite, pyrite and quartz indicate near-neutral pH
42 condition. $\delta^{34}\text{S}$ values, which vary from -1.1 to +3.9‰, suggest reduced conditions
43 when compared to the representative bulk $\delta^{34}\text{S}$ value for the Mankayan Mineral
44 District. The characteristics and conditions strongly indicate an intermediate sulfidation
45 epithermal (ISE) style of mineralization. Moreover, the $\delta\text{D}_{\text{water}}$ (-63 to -66‰) and
46 $\delta^{18}\text{O}_{\text{water}}$ (-3.9 to -1.1‰) values from the major vein-types suggest late stage formation
47 in a magmatic-hydrothermal system similar to other ISE deposits in the Northern Luzon
48 Segment (e.g., Victoria, Acupan and Antamok).

49 Given these, the presence of the Suyoc ISE veins in the underexplored southern
50 part of the Mankayan Mineral District implies potential presence of undiscovered
51 cogenetic porphyry Cu and high sulfidation epithermal mineralization in the area.

52 **1. Introduction**

53 The Mankayan Mineral District in Northern Luzon, Philippines is considered as
54 one of the most well-endowed districts in the Philippines in terms of hydrothermal
55 mineralization. It hosts some of the most well-known and well-studied hydrothermal
56 deposits, such as the Lepanto high sulfidation epithermal Cu-Au deposit (Claveria,
57 2001; Hedenquist et al., 2017), the Victoria intermediate sulfidation epithermal Au-Ag
58 deposit (Claveria, 2001; Sajona et al., 2002; Chang et al., 2011), and the Far Southeast
59 porphyry Cu-Au deposit (Shinohara and Hedenquist, 1997; Hedenquist et al., 1998;
60 2017). Other smaller deposits in the district include the Guinaoang porphyry Cu-Au
61 deposit (Sillitoe and Angeles, 1985) and Teresa epithermal Au-Ag vein deposit (Chang
62 et al., 2011). Several studies have been conducted in the district particularly on the Far
63 Southeast, Lepanto and Victoria deposits, which are considered to be genetically linked
64 due to their spatial and temporal relationships (e.g., Arribas et al., 1995; Hedenquist et
65 al., 1998; Chang et al., 2011).

66 However, there are still other significant mineralization in the district that need
67 to be investigated, as they may provide useful information in identifying other
68 porphyry-epithermal systems similar to the Far Southeast-Lepanto-Victoria. One of
69 these is the Suyoc prospect, which is situated at the less explored southern part of the
70 Mankayan district. The prospect has been mined by artisanal miners for its base metal-
71 rich veins consisting of quartz-carbonate-chalcopyrite (Gonzales, 1967) and is currently
72 managed by Itogon-Suyoc Resources Incorporated (ISRI). In this study, we present the
73 mineralization characteristics of the Suyoc prospect obtained from field investigation,
74 microscopy, fluid inclusion analysis, mineral chemistry analysis, and stable isotope
75 analysis. From these results, its formational conditions are constrained to determine its
76 mineralization style, and ultimately provide insights to the prospective potential of the
77 underexplored southern part of the Mankayan Mineral District.

78 **1.1. Regional Geologic Setting**

79 The Mankayan Mineral District is situated in the Northern Luzon Segment,
80 which forms part of the Taiwan-Luzon Arc that developed from the subduction of the
81 South China Sea Basin (SCSB) along the Manila Trench (e.g., Stephan et al., 1986;
82 Suppe, 1988; Teng, 1990) (Figure 1). The segment experienced major tectonic uplift
83 for the past 4 Ma as a consequence of the subduction of an extinct mid-oceanic ridge
84 manifested as the Scarborough Seamount Chain in the SCSB (Yang et al., 1996). The
85 subduction of this young and buoyant oceanic lithosphere resulted to the initiation of
86 subdued volcanism and emplacement of highly fertile andesite and dacite shallow
87 intrusions, which are considered to be responsible for the Pliocene-Pleistocene
88 hydrothermal mineralization in the Mankayan and Baguio Mineral Districts (e.g.,
89 Sajona and Maury, 1998; Cooke et al., 2005; Waters et al., 2011; Deng et al., 2020;
90 Jabagat et al., 2020).

91 The Luzon island is traversed from north to south by the left-lateral strike-slip
92 Philippine Fault Zone (PFZ). This seismically active fault zone in the Philippine Mobile
93 Belt was formed as a response to the northwestward convergence of the Philippine Sea
94 Plate and southeastward convergence of the Eurasian Plate (Aurelio, 2000; Queaño et
95 al., 2007; Armada et al., 2020). One of the northern splays of the PFZ, which is the
96 Abra River Fault (ARF), cuts the Northern Luzon Segment (Figure 1). The NS- to
97 NNW-trending ARF is a left-lateral fault with thrust component (Mines and
98 Geosciences Bureau (MGB), 2010). Its motion resulted to the formation of NW-
99 trending fault splays, which include the Lepanto fault, host to the Lepanto enargite
100 orebody (Maletterre, 1998). For that reason, the ARF is believed to have controlled the
101 spatial configuration of hydrothermal mineralization in the district (Chang et al., 2011;
102 Manalo et al., 2018).

103 **1.2. Mineralization in Mankayan Mineral District**

104 The Mankayan Mineral District has several hydrothermal deposits and
105 prospects within its ~25 km² area (Chang et al., 2011) (Figure 2a). The general age of
106 this district-wide mineralization is ~1.2 to 3.5 Ma (Arribas et al., 1995). The north-
107 central part hosts a well-defined porphyry-epithermal system composed of the Far
108 Southeast (FSE) porphyry Cu-Au deposit, the Lepanto high sulfidation epithermal
109 (HSE) Cu-Au deposit, and the Victoria intermediate sulfidation epithermal (ISE) Au-
110 Ag deposit. The FSE has a main mineralization stage associated with sericitic alteration
111 that overprints an earlier K-silicate alteration (Hedenquist et al., 1998). Its ore consists
112 of bornite, chalcopyrite and electrum (Concepción and Cinco, 1989), with Bi-Te-
113 bearing tennantite in several areas (Imai, 2000). Located on the shoulder of FSE is the
114 Lepanto HSE deposit. The main Lepanto orebody consists of early enargite-luzonite-
115 pyrite and late gold-telluride associated with tennantite-tetrahedrite. The orebody
116 occurs in vuggy quartz with haloes of alunite, kaolinite and dickite (Hedenquist et al.,
117 1998). On the other hand, the Victoria ISE deposit is situated a few hundred meters
118 southwest of the FSE (Chang et al., 2011). Victoria is characterized by chalcopyrite +
119 sphalerite + galena ± tennantite ± tetrahedrite sulfide assemblage and gold occurring as
120 native gold and electrum, with associated alteration of dominantly illite-chlorite
121 (Claveria, 2001). A recent study by Manalo et al. (2018) introduced the Northwest
122 quartz-pyrite-gold (QPG) vein mineralization located at the periphery of the main
123 Lepanto orebody. This mineralization occurred after the enargite-luzonite-pyrite stage
124 of Lepanto and is characterized by low-copper, high-gold epithermal veins mainly
125 hosted in the Cretaceous metavolcanic rocks.

126 Other significant porphyry mineralization in the district include the Guinaoang
127 porphyry Cu-Au deposit and the Buaki and Palidan porphyry prospects. The Guinaoang

128 deposit is located ~3 km southeast of the FSE and is characterized by Cu-Au
129 mineralization associated with K-silicate alteration overprinted with sericite-clay-
130 chlorite alteration (Sillitoe and Angeles, 1985). Sillitoe and Angeles (1985) reported an
131 advanced argillic cap on top of Guinaoang that has localized enargite mineralization.
132 The Buaki prospect is located ~2 km west of the FSE and is characterized by
133 outcropping porphyry-style stockworks, whereas the Palidan is a porphyry lithocap
134 prospect located ~2 km south of the Victoria deposit (Chang et al., 2011). Vein
135 prospects are also present and are mostly concentrated in the southern portion of the
136 district. These include the Teresa and Nayak prospects characterized by gold-bearing
137 base-metal veins (Chang et al., 2011).

138 **1.3. Local Geology**

139 The lithologies in the Mankayan Mineral District include metamorphic,
140 sedimentary, and volcano-plutonic rocks with ages from Late Cretaceous to Pleistocene
141 (Figure 2b). The basement in the area is the Late Cretaceous to Early Eocene Lepanto
142 Metavolcanics, which consists of indurated andesitic to basaltic lavas with minor
143 turbiditic sequences (Ringebach et al., 1990). Unconformable over the basement are
144 the Late Eocene to Early Oligocene Apaoan Volcaniclastics and Late Oligocene to
145 Early Miocene Balili Formation. The former is composed of green and red thin-bedded
146 siltstone-sandstone (Garcia, 1991), whereas the latter is characterized by thick
147 sequences of sandstones, volcanic conglomerates, basalt flows, andesitic pyroclastics
148 and breccia (Ringebach, 1992). The basement and the volcaniclastic rocks are intruded
149 by the Early to Middle Miocene Bagon Intrusive Complex dominantly consisting of
150 tonalite (Sillitoe and Angeles, 1985). This intrusive complex, together with the older
151 formations, is widely exposed at the western portion of the district. The Middle to Late
152 Miocene Suyoc Conglomerate unconformably overlies the older units and is exposed

153 at the southern area. The conglomerate is polymictic with clasts of well-rounded,
154 pebble- to cobble-sized chert, epidotized volcanic rocks and limestone (Gonzales,
155 1956). This conglomerate is overlain by the Pliocene to Pleistocene dacitic pyroclastic
156 rocks with associated dacitic dome complexes (Garcia and Bongolan, 1989). These
157 dacitic units are the Pliocene Imbanguila Dacite and the Pleistocene Bato Dacite (MGB,
158 2010). Both formations are widely exposed at the northeastern and east-central portions
159 of the district. On top of these dacitic units is the Lapangan Tuff, which consists of a
160 thin sequence of ash with an age of $18,820 \pm 670$ years based on C^{14} dating (Bureau of
161 Energy Development-Japan International Cooperation Agency, 1981).

162 **1.4. The Suyoc prospect**

163 The epithermal veins of the Suyoc prospect is hosted in the volcanoclastic rock
164 and conglomerate (Figure 2b). The volcanoclastic rock forms part of the Late Oligocene
165 to Early Miocene Balili Formation and consists of epiclastic sandstone and
166 conglomerate. The sandstone is a deformed bedded unit consisting of grains of lithic
167 andesite, amphibole, and plagioclase, whereas the matrix- to clast-supported
168 conglomerate is composed of cobble-sized clasts of aphanitic and porphyritic andesite
169 set in a partly silicified matrix (Figure 3a-3b). Overlying the Balili Formation is the
170 Suyoc Conglomerate. It consists of well-rounded, granule- to boulder-sized clasts of
171 andesite, porphyritic andesite, diorite, limestone, mudstone, and sandstone set in
172 dominantly andesitic, silt- to sand-sized matrix (Figure 3c-3d). The Suyoc
173 Conglomerate has a reported age of Middle to Late Miocene based on the dating of
174 foraminifera from a capping limestone (Gonzales, 1956; Maletterre, 1989). Capping the
175 exposures of the Suyoc Conglomerate is the Imbanguila Dacite Pyroclastics which was
176 dated 2.9 ± 0.40 Ma from the K-Ar dating of a biotite in a dacitic lapilli tuff (Sillitoe
177 and Angeles, 1985). The epithermal veins of the Suyoc prospect hosted in the Suyoc

178 Conglomerate terminate in this pyroclastic unit. Hence, considering such relationship,
179 the veins of the Suyoc prospect can be inferred to be younger than Late Miocene (Suyoc
180 Conglomerate) but older than Middle Pliocene (Imbanguila Dacite Pyroclastics).

181 A major structure in the area is the north-south trending lineament interpreted
182 herein as a possible southern extension of the Abra River Fault (Figure 2b). This major
183 fault was interpreted by other authors (e.g., Chang et al., 2011; Manalo et al., 2018) to
184 have influenced mineralization in the area. It may have also played a role in the
185 occurrence of structures that host the Suyoc epithermal veins.

186 **2. Methodology**

187 **2.1. Sample collection**

188 The field survey was conducted on accessible surface and underground vein
189 exposures in the Suyoc prospect. Underground exposures were observed by accessing
190 the portals of ISRI and small-scale miners (Figure 2a). Surface exposures are intensely
191 weathered that the primary characteristics of the veins were nearly unrecognizable.
192 Hence, megascopic description and identification were only conducted on veins in
193 accessed underground, where exposures are relatively well-preserved. Representative
194 vein samples, together with adjacent altered wall rock samples (within 5-meter
195 peripheral zone), were collected from the Esperanza, Elizabeth and Calixto tunnels at
196 depths of ~80 m, ~130 m and ~100 m from the present surface level, respectively
197 (Figure 2a).

198 **2.2. Petrography**

199 Polished slab-sections with thickness of ~5 mm were produced from the vein-
200 samples for petrographic analysis of opaque minerals (e.g., sulfides, Au). Double-
201 polished thin sections of ~30 μm thickness were also produced for petrographic analysis

202 of gangue minerals. The preparation of polished slab and double-polished thin sections
203 was done at the University of the Philippines – National Institute of Geological Sciences
204 (UP-NIGS) using a Pelcon Automatic Thin Section machine and a Topper Diamond
205 Polishing unit. Petrographic analysis was carried out using the Olympus BX53-P
206 polarizing microscope at UP-NIGS.

207 **2.3. Mineral chemistry analysis**

208 Gold-bearing minerals, and sphalerite crystals coexisting with pyrite were
209 subjected to mineral chemistry analysis. The Au-bearing minerals were analyzed for
210 Au and Ag composition, whereas sphalerite crystals were analyzed for Fe, Zn and S.
211 The slab-sections containing the desired minerals were coated with carbon using the
212 108C Auto Carbon Coater prior to analysis. Mineral chemistry analysis was done using
213 the JEOL JXA-8230 Electron Probe Microanalyzer at the University of the Philippines
214 – National Institute of Geological Sciences. Operating conditions were set to 15kV
215 acceleration voltage with probe current of 10 nA and probe diameter of 3-5 μm . Results
216 obtained were automatically calculated by JEOL software using ZAF correction matrix.
217 The final results are in mass percent values. Detection limits were calculated to range
218 from ~100-200 ppm.

219 **2.4. Fluid inclusion analysis**

220 Double-polished wafer samples of quartz with thickness ranging from 150-200
221 μm were prepared using similar equipment used for producing thin sections.
222 Microscopic analysis of fluid inclusions was conducted using the Olympus BX53-P
223 polarizing microscope at the University of the Philippines – National Institute of
224 Geological Sciences. Homogenization temperatures and final-ice melting temperatures
225 of the observed primary fluid inclusions were measured using the LINKAM 10002L

226 heating and cooling stage mounted in a Nikon Eclipse LV100N POL Microscope at the
227 Department of Earth Resources Engineering, Kyushu University, Japan. Salinity values
228 were calculated using the equation of Bodnar (1993) where θ is the final-ice melting
229 temperature:

$$230 \quad \text{Salinity (wt. \% NaCl equiv.)} = 0.00 + 1.78\theta - 0.0442\theta^2 + 0.000557\theta^3$$

231 **2.5. X-ray diffraction analysis**

232 Representative altered wall rock samples were subjected to X-ray diffraction
233 (XRD) analysis using bulk and oriented methods. For the bulk method, the samples
234 were powdered to $<10 \mu\text{m}$ using an agate mortar and pestle (e.g., Poppe et al., 2001).
235 The powdered samples were analyzed using the Rigaku Ultima IV XRD calibrated with
236 a silica standard at the Department of Earth Resources Engineering, Kyushu University,
237 Japan. For oriented method, samples were sonicated then subjected to centrifugation
238 technique to separate the clay components. Before subjecting these clay components to
239 XRD analysis, three treatments were applied to them: air drying, acid treatment using
240 HCl and glycolation using ethylene glycol.

241 **2.6. Stable isotope analysis**

242 Veins that contain recoverable quartz and pyrite crystals were slightly crushed
243 for oxygen-hydrogen and sulfur isotopic measurement, respectively. Quartz and pyrite
244 grains produced from crushing were separated by picking using stainless tweezers and
245 a binocular microscope. Pure grains of pyrite were recovered, but sulfide impurities
246 were observed in recovered quartz grains. Thus, purification using an aqua regia
247 solution was applied to remove the sulfides (e.g., Tindell et al., 2018). Stable isotope
248 analysis was carried out at the Scottish Universities Environmental Research Centre,
249 University of Glasgow. For oxygen isotope analysis, quartz separates were combusted

250 with CO₂ laser at temperature >1500°C with ClF₃ as the fluorinating agent (Sharp,
251 1990). The O₂ gas produced from combustion was reacted to hot graphite to convert O₂
252 to CO₂ and was subsequently analyzed using VG Optima mass spectrometer. For
253 hydrogen isotope analysis, quartz separates were heated to >700°C in a vacuum to
254 release fluids (Gleeson et al., 2008). Following the method of Donnelly et al. (2001),
255 the fluids were transformed to hydrogen by reaction with hot chromium and were
256 subsequently analyzed using the VG Optima mass spectrometer. Results in oxygen and
257 hydrogen isotope analyses are reported in δ₁₈O (‰) and δD (‰), respectively, relative
258 to the Standard Mean Ocean Water. For sulfur isotope analysis, liberation of SO₂ gas
259 was done by combusting the pyrite separates at 1075°C using Cu₂O as reagent
260 (Robinson and Kusakabe, 1975). Freed SO₂ gas was analyzed using VG Isotech SIRA
261 II mass spectrometer. Results are reported in δ³⁴S (‰) with respect to the Vienna Cañon
262 Diablo Troilite standard.

263 **3. Results**

264 **3.1. Vein-types, mineralogy and textures**

265 The epithermal veins of the Suyoc prospect are classified into three major types:
266 quartz vein, quartz-sulfide vein, and quartz-carbonate vein. The quartz vein is
267 characterized by anastomosing, massive veinlets (Figure 4a), which strike NE-SW and
268 N-S and dips 60-80°SE and 80°W, respectively. The adjacent wall rocks of this vein-
269 type are commonly intensely chloritized. Angular to sub-angular fragments of quartz
270 and intensely silicified wall rock are incorporated within the veins (Figure 5a). These
271 fragments often exhibit cockade texture characterized by bands of massive
272 microcrystalline quartz enclosing the wall rock fragments (Figure 6a). The vein
273 contains low amounts of pyrite and chalcopyrite (<1% vein volume) occurring as

274 disseminated anhedral crystals (<0.1 mm). This vein-type was observed in the Calixto,
275 Manuit and Antonio tunnels (Figure 2a).

276 The quartz-sulfide vein has a massive appearance with thickness that reaches
277 up to 0.5 m (Figure 4b). It generally strikes NE-SW and steeply dips to the SE and NW.
278 The vein is characterized by vuggy quartz with massive pyrite and chalcopyrite (Figure
279 5b). The quartz is micro- to macrocrystalline with massive and comb textures (Figure
280 6b). Disseminated pyrite and chalcopyrite make up ~10% of the sample. Subhedral
281 pyrite crystals have <1 mm diameter with presence of microfractures. Chalcopyrite has
282 a similar crystal size as pyrite but is mainly anhedral. It occurs as either infill in pyrite
283 microfractures or between pyrite crystals (Figure 6e). Minor sphalerite occurs as
284 intergrowth with chalcopyrite. This vein-type was observed in the Elizabeth and
285 Esperanza tunnels (Figure 2a).

286 The quartz-carbonate vein exhibits weak crustiform banding of quartz and
287 rhodochrosite. Its thickness rarely exceeds 0.3 m and occurs as continuous veins that
288 sometimes split into two or more branches. It strikes NE-SW and dips 75°NW and
289 63°NE. Oxidation affected the veins and host rocks that resulted to the formation of
290 malachite, Fe-Mn oxide encrustations and limonite film (Figure 4c). This vein-type is
291 mainly observed at the Elizabeth tunnel and less extensively at the Manuit tunnel. At
292 the Elizabeth tunnel, it crosscuts the quartz-sulfide vein (Figure 4d). The quartz and
293 rhodochrosite layers in this vein type exhibit asymmetric crustiform texture (Figure 5c).
294 The outer or marginal layer is composed of micro- to macrocrystalline quartz crystals
295 of massive texture (Figure 6c). Associated with this layer are intergrowth of pyrite,
296 chalcopyrite, galena, and sphalerite crystals with average diameters of ≤0.5 mm.
297 Sphalerite and galena often display interpenetrating boundaries. Chalcopyrite disease
298 is observed along the rim of sphalerite crystals (Figure 6f). Traces of bournonite

299 sulfosalts are observed as inclusions in galena (Figure 6g). Au-bearing minerals with
300 diameters of $<25\ \mu\text{m}$ commonly occur as inclusions in pyrite (Figure 6h) and
301 occasionally in chalcopyrite and sphalerite. Meanwhile, inner layer of the quartz-
302 carbonate vein is rhodochrosite that occurs as cryptocrystalline and macrocrystalline
303 variety. The cryptocrystalline rhodochrosite is situated in between the quartz layer and
304 the macrocrystalline rhodochrosite (Figure 6d). Very minor sphalerite and galena were
305 observed in the cryptocrystalline layer, whereas sulfides are absent in the
306 macrocrystalline layer.

307 Gypsum veins were also observed underground particularly in the Manuit
308 tunnel, but of unmapable extent (Figure 4e). They also outcrop on the surface where
309 they are associated with massive pyrite (Figure 4f).

310 **3.2. Elemental compositions**

311 Elemental compositions obtained from the mineral chemistry analysis of Au-
312 bearing minerals and sphalerite in the quartz-carbonate vein are shown in Table 1a and
313 1b, respectively. Sphalerite crystals that coexist with pyrite as indicated by their
314 interlocking relationship were selected for analysis.

315 The Au-bearing mineral 1 and 2 have elemental compositions diagnostic of
316 electrum, whereas 3 is of native gold composition (Figure 7). The 3 sphalerite crystals
317 have FeS mole percent values ranging from 0.51 to 8.30 (Figure 8). Sphalerite 1 has 8
318 analysis points, with the lowest values (< 1 FeS mole percent) recorded near the core
319 (Figure 8a). The subsequent point spikes to a value of 8.30 while the succeeding points
320 dropped to a lower value but still higher than that of the points near the core. Sphalerite
321 2, which has 5 analysis points, shows a similar trend where FeS mole percent values
322 are <1 near the core but increases up to about fourfold at the rim (Figure 8b). In

323 sphalerite 3, however, the core has a relatively high value with 1.02 FeS mole percent
324 while the 2 subsequent points toward the rim have values <1 (Figure 8c). The highest
325 value was recorded at the rim with a value of about twofold of that of the core. In
326 general, an apparent trend characterized by an increase in FeS content from the apparent
327 core to the apparent rim can be observed in the three sphalerite crystals of the quartz-
328 carbonate vein.

329 **3.3. Fluid inclusion petrography and microthermometry**

330 Quartz crystals from the three major vein-types were evaluated for fluid
331 inclusion petrography and microthermometry. For the quartz-carbonate vein, the
332 selected quartz crystals are those associated with Au-bearing minerals. Two groups of
333 liquid-rich inclusions were recognized from petrographic analysis. The first group
334 occurs in clusters, comprising of inclusions with sizes of <5 μm . These inclusions are
335 elongate in shape and have smooth boundaries and are thus interpreted to be of primary
336 type (Figure 9a, b) (Goldstein and Reynolds, 1994). Meanwhile, the second group is
337 composed of irregularly shaped isolated inclusions that had sizes ranging from 5 to 20
338 μm (Figure 9a, b). This group is interpreted as secondary type (Goldstein and Reynolds,
339 1994).

340 Primary fluid inclusions were analyzed in each vein-type. Their homogenization
341 temperature (T_h) values and computed salinity from final-ice melting temperature
342 values are listed in Table 2. Modal T_h values in the quartz vein and the quartz-carbonate
343 vein are within a narrow range of 240-250°C while the quartz-sulfide vein has a range
344 of 230-250°C. The modal salinity values have a general range of 1.0-3.5 wt. % NaCl
345 equivalent, with 2.5-3.5 in the quartz vein, 2.0-2.5 in the quartz-sulfide vein and 1.0-
346 1.5 in the quartz-carbonate vein. A positive correlation characterized by a decrease in

347 temperature with decrease in salinity can be inferred from the values of the quartz vein
348 (Figure 9c). Meanwhile, for the quartz-carbonate and quartz-sulfide veins, values are
349 quite scattered and has very weak correlation (Figure 9d, e).

350 **3.4. X-ray diffraction analysis**

351 Narrow alteration zones of around 5 to 10 meters typically surround the
352 epithermal veins of the Suyoc prospect. Results from X-ray diffraction analysis of these
353 alteration zones are shown in Figure 10. Bulk analysis of the altered wall rocks
354 associated with the three major vein-types revealed the presence of pyrite, quartz,
355 calcite, and phyllosilicate minerals such as clay and chlorite/kaolinite. The clay and
356 chlorite/kaolinite peaks detected in bulk analysis were further identified in oriented
357 analysis as illite and chlorite, respectively (Figure 10).

358 **3.5. Stable isotope composition**

359 Results of stable isotope analysis are shown in Table 3. The analyzed quartz
360 crystals are of the same variety as those assessed for fluid inclusion studies. $\delta^{18}\text{O}$ values
361 obtained are: +8.7‰ and +7.5‰ for the quartz vein, +5.6‰ and +5.5‰ for the quartz-
362 sulfide vein, and +7.8‰ and +7.7‰ for the quartz-carbonate vein. Corresponding δD
363 values derived from fluid inclusions are -65‰, -66‰ and -63‰, respectively.
364 Calculated $\delta^{18}\text{O}_{\text{water}}$ using the equation of Clayton et al. (1972) for 200-500°C quartz-
365 water system resulted in values of -0.7 to -0.2 and -1.9 to -1.4 for quartz vein, -4.4 to -
366 3.4 and -4.4 to -3.4 for quartz-sulfide vein, and -1.6 to -1.2 and -1.7 to -1.2 for quartz-
367 carbonate vein. Sulfur isotope data from pyrite of the quartz-carbonate vein and quartz-
368 sulfide vein revealed values of -1.1, -0.1‰ and 3.8, 3.9‰, respectively.

369 **4. Discussion**

370 **4.1. Conditions of formation**

371 The Suyoc epithermal veins are classified into three major types, namely the
372 quartz vein, quartz-sulfide vein, and quartz-carbonate vein. The gypsum vein, with
373 occasional presence of massive pyrite, also forms part of the prospect but is not
374 considered a major vein-type due to its limited extent and minor occurrence. The
375 summary of the characteristics of the three major vein-types that were obtained from
376 the analyses is shown in Table 4.

377 *4.1.1. Mechanism of deposition*

378 Homogenization temperature and salinity values from the three major vein-
379 types have modal range of 230-250°C and 1.0-3.5 wt.% NaCl equivalent, respectively.
380 These values are consistent to what is expected from an epithermal deposit (Bodnar et
381 al., 2014). Vein deposition in epithermal systems can be initiated by processes such as
382 boiling (e.g., Cooke et al, 1996; Moncada et al., 2012; 2017), fluid mixing (e.g., Vikre,
383 1989; Corbett and Leach, 1998), and wall rock interaction (e.g., Vennemann et al.,
384 1993; Cooke and McPhail, 2001). The major epithermal veins of the Suyoc prospect
385 predominantly display massive quartz texture associated with cockade in quartz vein,
386 comb in quartz-sulfide vein, and crustiform in quartz-carbonate vein. Massive and
387 comb textures can be interpreted as products of slow crystallization (e.g., Dong et al.,
388 1995; Moncada et al., 2012). Meanwhile, crustiform texture and its subtype, cockade
389 texture, may be interpreted as textures associated with fast crystallization (e.g., boiling)
390 when they coexist with rapidly-formed quartz textures like colloform and bladed,
391 among others (Simmons and Browne, 2000). However, the cockade and crustiform
392 textures exhibited by the quartz vein and quartz-sulfide vein, respectively, are
393 associated with massive quartz texture. This suggests that these cockade and crustiform
394 textures are associated with slow crystallization considering the massive texture's mode
395 of formation (e.g., Dong et al., 1995; Moncada et al., 2012). The dominance of liquid-

396 rich fluid inclusion hosted in quartz supports this apparently gradual crystallization
397 suggested by the quartz textures. Liquid-rich fluid inclusions are considered to be
398 entrapped during non-boiling condition, in which slow crystallization is typical (e.g.,
399 Bodnar et al., 1985; Moncada et al., 2012; 2017).

400 Evidence supporting the prevalence meteoric water dilution (or fluid mixing)
401 and wall rock interaction for the deposition of the veins in the Suyoc prospect are
402 present. In the quartz vein, apparent decrease in both homogenization temperature and
403 salinity as shown in Figure 9c suggests progressive dilution of hydrothermal fluid by
404 meteoric water (Wilkinson, 2001). In the quartz-carbonate vein, the occurrence of
405 rhodochrosite may also suggest mixing of marginal water (e.g., meteoric) into the
406 system to cause vein deposition (Simmons and Browne, 2000). The FeS content in the
407 sphalerite crystals of the quartz-carbonate vein is generally increasing from core to rim
408 (Figure 8). This progressive increase in FeS content signifies a progressive decrease in
409 sulfidation state, which can be considered to be a result of wall rock interaction (e.g.,
410 Barton et al., 1977; Einaudi et al., 2003).

411 *4.1.2. Sulfidation state*

412 In the epithermal veins of the Suyoc prospect, pyrite and chalcopyrite are
413 consistently present. These two sulfides represent the lower and upper stability limit of
414 intermediate sulfidation (IS) state in epithermal conditions, respectively (Einaudi et al.,
415 2003). Hence, the occurrence and coexistence of such sulfides in the epithermal veins
416 of the Suyoc prospect suggest an IS state. This is further supported by the FeS mole
417 percent values in the sphalerite crystals coexisting with pyrite. Obtained values range
418 from 0.51-8.30, which are well within the IS state considering a temperature of 240-
419 250°C from fluid inclusions (Figure 11) (Einaudi et al., 2003).

420 *4.1.3. pH condition*

421 The epithermal veins of the Suyoc prospect are associated with wall rock
422 alteration assemblage of illite, chlorite, pyrite, and quartz, with additional calcite
423 observed in the quartz-sulfide and quartz-carbonate veins. These alteration minerals
424 were formed under neutral pH condition in the epithermal environment (Figure 12)
425 (White and Hedenquist, 1995). Pyrite and quartz, although may overlap with acidic
426 condition, still indicate neutral pH condition in this case due to their coexistence with
427 neutral pH minerals (i.e., chlorite, illite, calcite).

428 *4.1.4. Redox condition*

429 According to Rye (1993), in a magmatic-hydrothermal system, variations in a
430 sulfide's $\delta^{34}\text{S}$ composition relative to the bulk sulfur isotope composition is a function
431 of both reduction-oxidation and temperature. The bulk composition represents the
432 composition of the cogenetic igneous rock or the hydrothermal fluid source (Rye,
433 1993). Sulfides precipitating from oxidized fluids ($\text{H}_2\text{S} < \text{SO}_2$) are expected to have
434 lower $\delta^{34}\text{S}$ values relative to the bulk composition, with $\delta^{34}\text{S}$ values becoming
435 progressively lower as temperature decreases, whereas sulfides precipitating from
436 reduced fluids ($\text{H}_2\text{S} > \text{SO}_2$) only undergo minimal decrease in $\delta^{34}\text{S}$ values regardless of
437 temperature, resulting to $\delta^{34}\text{S}$ values not varying much from the bulk composition (Rye,
438 1993; 2005). Having such concept, it is important to know the bulk sulfur isotope
439 composition representative for the Suyoc prospect in order to interpret its $\delta^{34}\text{S}$ values
440 then constrain its redox condition.

441 Imai (2000) and Manalo et al. (2018) have reported a +5‰ bulk sulfur isotope
442 composition for the hydrothermal mineralization in the Mankayan Mineral District
443 (MMD) in which the Suyoc prospect is situated. This value is in agreement with those

444 in subduction-related volcanic arcs (Sasaki and Ishihara, 1979). Hence, for the
445 interpretation of the $\delta^{34}\text{S}$ value of the Suyoc prospect, the +5‰ value suggested by Imai
446 (2000) and Manalo et al. (2018) is used here. An estimated $\delta^{34}\text{S}$ compositional
447 evolution in sulfide through reduced and oxidized cooling pathways in reference to
448 +5‰ bulk composition is shown in Figure 13. In the figure, it can be observed that the
449 $\delta^{34}\text{S}$ values (-1.1 to +3.9‰) of the Suyoc quartz-sulfide and quartz-carbonate veins and
450 their corresponding temperatures plot within the reduced path suggesting the deposition
451 of both veins under reduced condition ($\text{H}_2\text{S} > \text{SO}_2$). It is known that mineralizing
452 hydrothermal fluids, which separate from porphyry intrusions in magmatic arcs such as
453 in MMD, are originally oxidized ($\text{H}_2\text{S} > \text{SO}_2$) (e.g., Sun et al., 2015; Deng et al., 2017;
454 Zhang et al., 2017). The reduced condition exhibited by the quartz-sulfide and quartz-
455 carbonate veins is likely to be caused by the progressive oxygen buffering of fluids by
456 wall rock during ascent (Einaudi et al., 2003; Sillitoe and Hedenquist, 2003). The
457 occurrence of gypsum veins in the Suyoc prospect, which accounts for the introduction
458 of oxidized fluid (Hedenquist et al., 2000), can be hypothesized as a product of later
459 veining stage when the buffering capacity of the wall rock is already exhausted. This is
460 similar to other epithermal vein systems in the Northern Luzon Segment showing late
461 stage deposition of sulfate minerals (e.g., Victoria deposit: Claveria, 2001; Acupan
462 deposit: Cooke et al., 1996).

463 **4.2. Mineralization style**

464 The conditions of formation of the three major vein-types of the Suyoc prospect
465 conform to typical intermediate sulfidation epithermal (ISE) style of mineralization.
466 Sulfide mineralogy from the three major vein-types, as well as FeS content in sphalerite
467 in the quartz-carbonate vein, indicates that the fluid was at intermediate sulfidation
468 state. Alteration mineralogy of illite, chlorite, with associated pyrite, quartz, and calcite,

469 signifies neutral pH fluid condition. Sulfur isotope values recorded in pyrite suggest
470 reduced condition during base and precious metal deposition (i.e., quartz-sulfide vein
471 and quartz-carbonate vein). These constrained fluid conditions are consistent with
472 fluids that form ISE mineralization (Sillitoe and Hedenquist, 2003; Einaudi et al.,
473 2003). In addition, one of the characteristics displayed by the Suyoc prospect that is
474 typical to an ISE endmember is the occurrence of rhodochrosite- and gypsum-bearing
475 veins, which is a characteristic of typical ISE deposit (e.g., Victoria deposit,
476 Philippines: Claveria, 2001; Cayloma deposit, Peru: Echavarria et al., 2006).

477 Presence of ISE deposits is well-documented in the Northern Luzon Segment.
478 The Victoria ISE deposit (e.g., Claveria, 2001; Chang et al., 2011) north of the Suyoc
479 prospect, and the Acupan ISE vein system in Baguio Mineral District (Cooke et al.,
480 1996), are the best examples. The occurrence of ISE style mineralization in the
481 Northern Luzon Segment can be attributed to its compressive island arc setting (Sillitoe
482 and Hedenquist, 2003; Garwin et al., 2005).

483 **4.3. Timing of formation**

484 As discussed in the previous section, the epithermal veins of the Suyoc prospect
485 belong to the ISE style. ISE mineralization typically occurs in a magmatic-
486 hydrothermal system, in which high sulfidation epithermal (HSE) and porphyry Cu
487 mineralization may co-occur (Sillitoe and Hedenquist, 2003; Einaudi et al., 2003). The
488 theoretical model developed by Shinohara and Hedenquist (1997) about the magma
489 degassing involved during the formation and evolution of the Far Southeast (FSE)
490 porphyry Cu-Au deposit provides a better understanding of the formational timing of
491 specific alteration and mineralization in a magmatic-hydrothermal system. Their model
492 displays the importance of δD value as one of the proxies on determining such timings.

493 According to Shinohara and Hedenquist (1997), two distinct single-phased
494 liquids were involved in the FSE magmatic-hydrothermal system: the early high
495 temperature liquid with δD of about -25‰, and the late low temperature liquid with δD
496 of about -40‰. More detail about these two liquids is shown in Figure 14a. The early
497 high temperature liquid dissociated to vapor and hypersaline liquid to form advanced
498 argillic and potassic alteration, respectively; whereas the late low temperature liquid
499 formed sericitic alteration that is associated with the main precious- and base-metal
500 mineralization (Shinohara and Hedenquist, 1997; Hedenquist et al., 1998). Hedenquist
501 et al. (1998) provided detailed isotopic composition for the advanced argillic alteration,
502 which represents the vapor, and the sericitic alteration, which represents the mineralized
503 late low temperature liquid. The meteoric water mixing trends of these two fluids, the
504 vapor and the late low temperature liquid, relatively differ, as the former is a product
505 of the earlier, high δD value liquid, whereas the latter came from the later, low δD value
506 source (Figure 14b).

507 Looking into the δD values of the Suyoc prospect from the quartz of the three
508 major vein-types, the values indicate a source that is low in heavy hydrogen isotope.
509 Such composition can also be observed in other ISE mineralization in the Northern
510 Luzon Segment, which are Acupan and Antamok of the Baguio Mineral District
511 (Sawkins et al., 1979). The low δD values of the Suyoc prospect and the Acupan-
512 Antamok show resemblance to that of the late low temperature liquid of the FSE (Figure
513 14b). This suggests that the formation of these ISE mineralization occurred at the later
514 stage of their respective magmatic-hydrothermal system. Such timing is consistent with
515 the late mineralization stage of the FSE magmatic-hydrothermal system that formed the
516 porphyry Cu, Lepanto HSE (Shinohara and Hedenquist, 1997; Hedenquist et al., 1998),
517 and perhaps the cogenetic Victoria ISE (e.g., Claveria, 2001; Chang et al., 2011).

518 **4.4. Exploration Implications**

519 It is widely accepted that ISE mineralization typically exists with porphyry Cu
520 and HSE mineralization in subduction-related magmatic arcs under near-neutral, mildly
521 extensional, or compressive stress regime (e.g., Hedenquist et al., 1998; Sillitoe and
522 Hedenquist, 2003; Chang et al., 2011; Wang et al., 2019). The MMD in Northern Luzon
523 Segment is no stranger to such kind of mineralization associations considering its
524 tectonic setting (e.g., Sajona and Maury, 1998; Cooke et al., 2005; Waters et al., 2011;
525 Deng et al. 2020; Jabagat et al., 2020). The prime example to it is the Far Southeast-
526 Lepanto-Victoria porphyry-epithermal system, which is just ~3 km north of the Suyoc
527 prospect (Chang et al., 2011).

528 Considering the prominence of porphyry-epithermal systems in MMD, the
529 existence of the Suyoc ISE veins does imply potential presence of cogenetic porphyry
530 Cu and HSE mineralization in its vicinity (Figure 15). The neighboring Victoria ISE
531 deposit displays a spatial configuration that is at least ~1 km away from its cogenetic
532 Far Southeast porphyry Cu-Au and Lepanto HSE deposits (Chang et al., 2011).
533 Following this configuration, an ~1 km radius of prospective area can be proposed
534 around the Suyoc prospect for potential presence of porphyry Cu and HSE
535 mineralization (Figure 16). Investigation for the presence of lithocap or advanced
536 argillic alteration is highly recommended in this prospective area, as this strongly
537 signifies potential presence of HSE and underlying porphyry (e.g., Sillitoe, 2010,
538 Chang et al., 2011).

539 **5. Conclusions**

540 This study presents the following mineralization characteristics and formational
541 conditions for the epithermal veins of the Suyoc prospect:

- 542 1) The veins are mainly hosted in the Middle to Late Miocene Suyoc
543 Conglomerate and Late Oligocene to Early Miocene Balili Formation.
- 544 2) The veins are classified into three major types: quartz vein, quartz-sulfide vein,
545 and quartz-carbonate vein. Quartz vein consists of massive and cockade quartz
546 with pyrite + chalcopyrite. Quartz-sulfide vein is characterized by massive and
547 comb quartz with pyrite + chalcopyrite + sphalerite. Quartz-carbonate vein is
548 characterized by massive quartz with rhodochrosite and chalcopyrite +
549 sphalerite + galena + Au/Ag ± bournonite. In addition, there is a minor vein-
550 type of gypsum ± pyrite composition.
- 551 3) The general temperature of formation of the veins range from 230-250°C and
552 salinity of 1.0-3.5 wt. % NaCl equivalent. Quartz textures (e.g., massive,
553 cockade, comb, crustiform) and dominance of liquid-rich fluid inclusion
554 suggest the prevalence of non-boiling mechanism of vein deposition. These
555 non-boiling processes are inferred as meteoric water dilution based on
556 homogenization versus salinity trend in quartz vein and presence of
557 rhodochrosite in quartz-carbonate vein, and wall rock interaction based on FeS
558 trend in sphalerite crystals of quartz-carbonate vein.
- 559 4) The sulfide assemblage containing pyrite and chalcopyrite and FeS mole
560 percent range of 0.51 to 8.30 indicate intermediate-sulfidation state. Alteration
561 assemblage of illite chlorite, pyrite, quartz with calcite indicates near-neutral
562 pH condition. $\delta^{34}\text{S}$ values from -1.1 to +3.9‰ suggest reduced condition when
563 compared to the representative bulk $\delta^{34}\text{S}$ value for the Mankayan Mineral
564 District. These characteristics and conditions strongly point to an intermediate
565 sulfidation epithermal style.

566 5) δD_{water} (-63 to -66‰) and $\delta^{18}O_{\text{water}}$ (-3.9 to -1.1‰) values suggest late stage
567 formation in the magmatic-hydrothermal system, consistent with other
568 intermediate sulfidation epithermal mineralization in the Northern Luzon
569 Segment (e.g., Victoria, Acupan and Antamok).

570 The presence of the Suyoc intermediate sulfidation epithermal veins implies a
571 potential presence of undiscovered cogenetic porphyry Cu and high sulfidation
572 epithermal mineralization in the underexplored southern part of the Mankayan Mineral
573 District.

574 **Acknowledgements**

575 We would like to express our gratitude to the Itogon-Suyoc Resources
576 Incorporated (ISRI) for logistical support and access to the Suyoc prospect. Members
577 of the Rushurgent Working Group are also thanked for their fieldwork assistance and
578 their contribution to this study through scientific discussions. The Department of
579 Science and Technology (Philippines) provided the funding support for the Electron
580 Probe Microanalyzer used in this study. This research is partially funded by the
581 University of the Philippines Office of the Vice Chancellor for Research and
582 Development (OVCRD) through the Outright Research Grant to JA Gabo-Ratio. We
583 would also like to thank the comments and inputs of an anonymous reviewer and Dr.
584 Adi Maulana to improve the manuscript.

585 **References**

586 Armada, L.T., Hsu, S.-k., Dimalanta, C.B., Yumul, G.P., Jr., Doo, W.-b., Yeh, Y.-c.,
587 2000. Forearc structures and deformation along the Manila Trench. *Journal of*
588 *Asian Earth Sciences* 4, 100036. <https://doi.org/10.1016/j.jaesx.2020.100036>.

589 Arribas, A., Jr., Hedenquist, J.W., Itaya, T., Okada, T., Concepción, R.A., Garcia, J.S.,
590 Jr., 1995. Contemporaneous formation of adjacent porphyry and epithermal Cu-
591 Au deposits over 300 ka in northern Luzon, Philippines. *Geology* 23, 337-340.
592 [https://doi.org/10.1130/0091-7613\(1995\)023<0337:CFOAPA>2.3.CO;2](https://doi.org/10.1130/0091-7613(1995)023<0337:CFOAPA>2.3.CO;2).

593 Aurelio, M.A., 2000. Shear partitioning in the Philippines: Constraints from Philippine
594 fault and global positioning system data. *Island Arc* 9, 584–597.
595 <https://doi.org/10.1111/j.1440-1738.2000.00304.x>.

596 Barton, P. B., Jr., Bethke, P.M., Roedder, E., 1977. Environment of ore deposition in
597 the Creede mining district, San Juan Mountains, Colorado: Part III. Progress
598 toward interpretation of the chemistry of the ore-forming environment.
599 *Economic Geology* 72, 1-24. <https://doi.org/10.2113/gsecongeo.72.1.1>.

600 Barton, P.B., Jr., Toulmin, P., 1966. Phase relations involving sphalerite in the Fe-Zn-
601 S system. *Economic Geology* 61, 815–849.
602 <https://doi.org/10.2113/gsecongeo.61.5.815>.

603 Bodnar, R.J., 1993. Revised equation and table for determining the freezing point
604 depression of H₂O-NaCl solutions. *Geochimica et Cosmochimica Acta* 57, 683-
605 684. [https://doi.org/10.1016/0016-7037\(93\)90378-A](https://doi.org/10.1016/0016-7037(93)90378-A).

606 Bodnar, R.J., Lecumberri-Sanchez, P., Moncada, D., Steele-MacInnis, M., 2014. Fluid
607 inclusions in hydrothermal ore deposits. *Treatise on Geochemistry*, 2nd ed.,
608 119-142. <https://doi.org/10.1016/B978-0-08-095975-7.01105-0>.

609 Bodnar, R.J., Reynolds, T.J., Kuehn, C.A., 1985. Fluid-inclusion systematics in
610 epithermal systems. *Reviews in Economic Geology* 2, 73-97.
611 <https://doi.org/10.5382/Rev.02.05>.

612 Bureau of Energy Development-Japan International Cooperation Agency, 1981. Report
613 on Buguias geothermal development. Phase I: BED Report No. 12, MPN.

614 Chang, Z., Hedenquist, J.W., White, N.C., Cooke, D.R., Roach, M., Deyell, C.L.,
615 Garcia, J.S., Jr., Gemmell, J.B., McKnight, S., Cuisson, A.L., 2011. Exploration
616 tools for linked porphyry and epithermal deposits: Example from the Mankayan
617 intrusion-centered Cu-Au district, Luzon, Philippines. *Economic Geology* 106,
618 1365-1398. <https://doi.org/10.2113/econgeo.106.8.1365>.

619 Claveria, R.J.R., 2001. Mineral paragenesis of the Lepanto copper and gold and the
620 Victoria gold deposits, Mankayan mineral district, Philippines. *Resource*
621 *Geology* 51, 97-106. <https://doi.org/10.1111/j.1751-3928.2001.tb00084.x>.

622 Clayton, R.N., O'Neil, J.R., Mayeda, T.K., 1972. Oxygen isotope exchange between
623 quartz and water. *Journal of Geophysical Research* 77, 3057–3067.
624 <https://doi.org/10.1029/JB077i017p03057>.

625 Concepción, R.A., Cinco, J.C., Jr., 1989. Geology of Lepanto Far Southeast gold-rich
626 porphyry copper deposit, Mankayan, Benguet, Philippines [abs.]: International
627 Union of Geological Sciences, International Geological Congress, 28th,
628 Washington, D.C., USA, 1989, Abstract Volume 1, 318–320.

629 Cooke, D.R., McPhail, D.C., 2001. Epithermal Au-Ag-Te Mineralization, Acupan,
630 Baguio District, Philippines: Numerical Simulations of Mineral Deposition.
631 *Economic Geology* 96, 109-131. <https://doi.org/10.2113/gsecongeo.96.1.109>.

632 Cooke, D.R., McPhail, D.C., Bloom, M.S., 1996. Epithermal gold mineralization,
633 Acupan, Baguio district, Philippines: geology, mineralization, alteration and the
634 thermochemical environment of ore deposition. *Economic Geology* 91, 243–
635 272. <https://doi.org/10.2113/gsecongeo.91.2.243>.

- 636 Cooke, D.R., Hollings, P., Walshe, J.L., 2005. Giant porphyry deposits: Characteristics,
637 distribution and tectonic controls. *Economic Geology* 100, 801–818.
638 <https://doi.org/10.2113/gsecongeo.100.5.801>.
- 639 Corbett, GJ., Leach, T.M., 1998. Southwest Pacific rim gold-copper systems: Structure,
640 alteration and mineralization. *Society of Economic Geologists Special*
641 *Publication* 6, 237. <https://doi.org/10.5382/SP.06>.
- 642 Deng, J.H., Yang, X.Y., Qi, H.S., Zhang, Z.-f., Mastoi, A.S., Sun, W.D., 2017. Early
643 Cretaceous high-Mg adakites associated with Cu-Au mineralization in the Cebu
644 Island, Central Philippines: Implication for partial melting of the paleo-Pacific
645 Plate. *Ore Geology Reviews* 88, 251-269.
646 <https://doi.org/10.1016/j.oregeorev.2017.05.006>.
- 647 Deng, J.H., Yang, X.Y., Zhang, L.-p., Duan, L.A., Mastoi, A.S., Liu, H., 2020. An
648 overview on the origin of adakites/adakititic rocks and related porphyry Cu-Au
649 mineralization, Northern Luzon, Philippines. *Ore Geology Reviews* 124,
650 103610. <https://doi.org/10.1016/j.oregeorev.2020.103610>.
- 651 Dong, G., Morrison, G., Jaireth, S., 1995. Quartz textures in epithermal veins,
652 Queensland – classification, origin, and implication. *Economic Geology* 90,
653 1841-1856. <https://doi.org/10.2113/gsecongeo.90.6.1841>.
- 654 Donnelly, T., Waldron, S., Tait, A., Dougans, J., Bearhop, S., 2001. Hydrogen isotope
655 analysis of natural abundance and deuterium enriched waters by reduction over
656 chromium on-line to a dynamic dual inlet isotope ratio mass spectrometer.
657 *Rapid Communications in Mass Spectrometry* 15, 1297–1303.
658 <https://doi.org/10.1002/rcm.361>.

659 Echavarria, L., Nelson, E., Humphrey, J., Chavez, J., Escobedo, L., Iriondo, A., 2006.
660 Geologic evolution of the Caylloma epithermal vein district, southern Peru.
661 Economic Geology 101, 843-863.
662 <https://doi.org/10.2113/gsecongeo.101.4.843>.

663 Einaudi, M.T., Hedenquist, J.W., Inan, E.E., 2003. Sulfidation state of fluids in active
664 and extinct hydrothermal systems: Transitions from porphyry to epithermal
665 environments. Society of Economic Geologists Special Publication 10, 285-
666 314. <https://doi.org/10.5382/SP.10.15>.

667 Garcia, J.S., 1991. Geology and mineralization characteristics of the Mankayan mineral
668 district, Benguet, Philippines. Geological Survey of Japan Report 277, 21–30.

669 Garcia, J.S., Bongolan, M.B., 1989. Developments in enargite ore search at Lepanto,
670 Mankayan, Benguet, Philippines [ext. abs.]: Philippine Mine Safety
671 Association, Symposium on Mineral Resource Development, Manila,
672 Philippines, 1989, Conference Proceedings, 1–21.

673 Garwin, S., Hall, R., Watanabe, Y., 2005. Tectonic setting, geology, and gold and
674 copper mineralization in Cenozoic Magmatic Arcs of Southeast Asia and the
675 West Pacific. Economic Geology 100th Anniversary, 891-930. Giggenbach,
676 W.F., 1992. Magma degassing and mineral deposition in hydrothermal systems
677 along convergent plate boundaries. Economic Geology 87, 1927–1944.
678 <https://doi.org/10.5382/AV100.27>.

679 Gleeson, S.A., Roberts, S., Fallick, A.E., Boyce, A.J., 2008. Micro-Fourier Transform
680 Infrared (FT-IR) and δD value investigation of hydrothermal vein quartz:
681 Interpretation of fluid inclusion δD values in hydrothermal systems.

682 Geochimica et Cosmochimica Acta 72, 4595–4606.
683 <https://doi.org/10.1016/j.gca.2008.06.014>.

684 Goldstein, R.H., Reynolds, T.J., 1994. Systematics of fluid inclusions in diagenetic
685 minerals. Society of Sedimentary Geologists Short Course 31, 199 pp.

686 Gonzales, A.G., 1956. The Lepanto Copper Mine. In: Copper Deposits of the
687 Philippines (Edited by A. R. Kinkel et al.). Philippine Bureau of Mines SPS 16.

688 Gonzalez, A.G., 1967. Copper-gold mineralization in the Mankayan-Suyoc district,
689 Mountain Province. Proceedings of the Second Geological Convention and 1st
690 Symposium on the Geology of the Mineral Resources of the Philippines and
691 Neighboring Countries, January 11–14, 1967, v. 2, p. 260.

692 Hedenquist, J.W., Arribas, A.R., Aoki, M., 2017. Zonation of sulfate and sulfide
693 minerals and isotopic composition in the Far Southeast Porphyry and Lepanto
694 epithermal Cu-Au deposits, Philippines. *Resource Geology* 67, 174-196.
695 <https://doi.org/10.1111/rge.12127>.

696 Hedenquist, J.W., Arribas, A., Jr., Gonzalez-Urien, E., 2000. Exploration for
697 epithermal gold deposits. *Economic Geology* 13, 245–277.
698 <https://doi.org/10.5382/Rev.13.07>.

699 Hedenquist, J.W., Arribas, A.R., Reynolds, T.J., 1998. Evolution of an intrusion-
700 centered hydrothermal system: Far Southeast-Lepanto porphyry and epithermal
701 Cu-Au deposits, Philippines. *Economic Geology* 93, 373-404.
702 <https://doi.org/10.2113/gsecongeo.93.4.373>.

703 Imai, A., 2000. Mineral paragenesis, fluid inclusions and sulfur isotope systematics of
704 the Lepanto Far Southeast porphyry Cu-Au deposit, Mankayan, Philippines.

705 Resource Geology 50, 151-168. <https://doi.org/10.1111/j.1751->
706 3928.2000.tb00065.x.

707 Jabagat, K.D., Gabo-Ratio, J.A., Queaño, K.L., Yonezu, K., Dimalanta, C.B., Lee,
708 Y.H., Yumul, G.P., Jr., 2020. Petrogenetic constraints on magma fertility in the
709 Baguio Mineral District, Philippines: Probing the mineralization potential of the
710 igneous host rocks in the Sangilo epithermal deposit. *Ore Geology Reviews*
711 125, 103703. <https://doi.org/10.1016/j.oregeorev.2020.103703>.

712 Japan International Cooperation Agency (JICA), 1984. Report on Acupan-Itogon
713 geothermal development. Second Phase Survey: Tokyo, Japan International
714 Cooperation Agency, 123.

715 Maletterre, P., 1989. Histoire, sedimentation, magmatique, tectonique et metallogenique
716 d'un arc oceanique deforme en regime de transpression. Doctoral Dissertation:
717 Universite de Bretagne Occidentale, 304 pp.

718 Manalo, P.C., Imai, A., Subang, L.L., de los Santos, M.C., Yanagi, K., Takahashi, R.,
719 Blamey, N.J.F., 2018. Mineralization of the Northwest quartz-pyrite-gold veins:
720 Implications for multiple mineralization events at Lepanto, Mankayan Mineral
721 District, Northern Luzon, Philippines. *Economic Geology* 113, 1609-1626.
722 <https://doi.org/10.5382/econgeo.2018.4606>.

723 Mines and Geosciences Bureau (MGB), 2010. *Geology of the Philippines* 2nd ed.,
724 Mines and Geosciences Bureau, North Avenue, Quezon City, Philippines.

725 Moncada, D., Baker, D., Bodnar, R.J., R.J., 2017. Mineralogical, petrographic and fluid
726 inclusion evidence for the link between boiling and epithermal Ag-Au
727 mineralization in La Luz area, Guanajuato Mining District, Mexico. *Ore*

728 Geology Reviews 89, 143-170. [https://doi.org/](https://doi.org/10.1016/j.oregeorev.2017.05.024)
729 10.1016/j.oregeorev.2017.05.024.

730 Moncada, D., Mutchler, S., Nieto, A., Reynold, T.K., Rimstidt, J.D., Bodnar, R.J.,
731 2012. Mineral textures and fluid inclusion petrography of the epithermal Ag-
732 Au deposits at Guanajuato, Mexico: Application to exploration. *Journal of*
733 *Geochemical Exploration* 114, 20-35.
734 <https://doi.org/10.1016/j.gexplo.2011.12.001>.

735 Poppe, L.J., Paskevich, V.F., Hathaway, J.C., Blackwood, D.S., 2001. A laboratory
736 manual for X-ray powder diffraction. USGS Report 01-041.

737 Queaño, K.L., Ali, J.R., Milsom, J., Aitchison, J.C., Pubellier, M., 2007. North Luzon
738 and the Philippine Sea Plate motion model: insights following paleomagnetic,
739 structural, and age-dating investigations. *Journal of Geophysical Research* 112,
740 1–44. <https://doi.org/10.1029/2006JB004506>.

741 Ringenbach, J.C., 1992. La Faille Philippine et les chaînes en décrochement associés
742 (centre et nord de Luzon): Evolution cénozoïque et cinématique des
743 déformations quaternaires. Doctoral Dissertation: Universite de Nice, 316 pp.

744 Ringenbach, J.C., Stephan, J.F., Maletierre, P., Bellon, H., 1990. Structure and
745 geological history of the Lepanto-Cervantes releasing bend in the Abra River
746 Fault, Luzon Central Cordillera, Philippines. *Tectonophysics* 183, 225-241.
747 [https://doi.org/10.1016/0040-1951\(90\)90418-8](https://doi.org/10.1016/0040-1951(90)90418-8).

748 Robinson, B.W., Kusakabe, M., 1975. Quantitative preparation of sulfur dioxide, for
749 34S/32S analyses, from sulfides by combustion with cuprous oxide. *Analytical*
750 *Chemistry* 47, 1179–1181. <https://doi.org/10.1021/ac60357a026>.

- 751 Rye, R.O., 1993. The evolution of magmatic fluids in the epithermal environment:
752 stable isotope perspective. *Economic Geology* 88, 733-753.
753 <https://doi.org/10.2113/gsecongeo.88.3.733>.
- 754 Rye, R.O., 2005. A review of the stable-isotope geochemistry of sulfate minerals in
755 selected igneous environments and related hydrothermal systems. *Chemical*
756 *Geology* 215, 5-36. <https://doi.org/10.1016/j.chemgeo.2004.06.034>.
- 757 Sajona, F.G., Izawa, E., Motomura, Y., Imai, A., Sakakibara, H., Watanabe, K., 2002.
758 Victoria carbonate-base metal gold deposit and its significance in the Mankayan
759 mineral district, Luzon, Philippines. *Resource Geology* 52, 315-328.
760 <https://doi.org/10.1111/j.1751-3928.2002.tb00142.x>.
- 761 Sajona, F.G., Maury, R.C., 1998. Association of adakites with gold and copper
762 mineralization in the Philippines. *Earth and Planetary Science Letters* 326, 27-
763 34. [https://doi.org/10.1016/S1251-8050\(97\)83200-4](https://doi.org/10.1016/S1251-8050(97)83200-4).
- 764 Sasaki, A., Ishihara, S., 1979. Sulfur isotopic composition of the magnetite-series and
765 ilmenite-series granitoids in Japan. *Contribution to Mineralogy and Petrology*
766 68, 107-115. <https://doi.org/10.1007/BF00371893>.
- 767 Sawkins, F.J., O'Neill, J.R., Thompson, J.M., 1979. Fluid inclusion and geochemical
768 studies of vein gold deposits, Baguio district, Philippines. *Economic Geology*
769 74, 1420-1434. <https://doi.org/10.2113/gsecongeo.74.6.1420>.
- 770 Sharp, Z.D., 1990. A laser-based microanalytical method for the in-situ determination
771 of oxygen isotope ratios of silicates and oxides. *Geochimica et Cosmochimica*
772 *Acta* 54, 1353–1357. [https://doi.org/10.1016/0016-7037\(90\)90160-M](https://doi.org/10.1016/0016-7037(90)90160-M).

- 773 Shinohara, H., Hedenquist, J.W., 1997. Constraints on magma degassing beneath the
774 Far Southeast porphyry Cu-Au deposit, Philippines. *Journal of Petrology* 38,
775 1741–1752. <https://doi.org/10.1093/petroj/38.12.1741>.
- 776 Sillitoe, R.H. (2010). Porphyry copper systems. *Economic Geology* 105, 3-41.
777 <https://doi.org/10.2113/gsecongeo.105.1.3>.
- 778 Sillitoe, R.H., Angeles, C.A., Jr., 1985. Geological characteristics and evolution of a
779 gold-rich porphyry copper deposit at Guinaoang, Luzon, Philippines. *Asian*
780 *Mining '85*, Manila, Philippines, February 11-14, Institute of Mining and
781 Metallurgy, London, 15-26.
- 782 Sillitoe, R.H., Hedenquist, J.W., 2003. Linkages between volcanotectonic settings, ore-
783 fluid compositions, and epithermal precious-metal deposits. *Economic Geology*
784 10, 315-343. <https://doi.org/10.5382/SP.10.16>.
- 785 Simmons, S.F., Browne, P.R.L., 2000. Hydrothermal minerals and precious metals in
786 the Broadlands-Ohaaki Geothermal System: Implications for understanding
787 low-sulfidation epithermal environments. *Economic Geology* 95, 971–999.
788 <https://doi.org/10.2113/gsecongeo.95.5.971>.
- 789 Stephan, J.F., Blanchet, R., Rangin, C., Pelletier, B., Letouzey, J., Muller, C., 1986.
790 Geodynamic evolution of the Taiwan-Luzon Mindoro belt since the late
791 Eocene. *Tectonophysics* 125, 245-268. [https://doi.org/10.1016/0040-](https://doi.org/10.1016/0040-1951(86)90017-X)
792 [1951\(86\)90017-X](https://doi.org/10.1016/0040-1951(86)90017-X).
- 793 Sun, W.D., Huang, R.-f., Li, H., Hu, Y.-b., Zhang, C.-c., Sun, S.-j., Zhang, L.-p., Ding,
794 X., Li, C.-y., Zartman, R.E., 2015. Porphyry deposits and oxidized magmas.
795 *Ore Geology Reviews* 65, 97-131.
796 <https://doi.org/10.1016/j.oregeorev.2014.09.004>.

797

798 Suppe, J., 1988. Tectonics of arc-continent collision on both sides of the South China
799 Sea: Taiwan and Mindoro. *Acta Geologica Taiwanica* 26, 1-18.

800 Taylor, B.E., 1992. Degassing of H₂O from rhyolite magma during eruption and
801 shallow intrusion, and the isotopic composition of magmatic water in
802 hydrothermal systems. *Japan Geological Survey Report* 279, 190–194.

803 Teng, L.S., 1990. Geotectonic evolution of late Cenozoic arc continent collision in
804 Taiwan. *Tectonophysics* 183, 57-76. [https://doi.org/10.1016/0040-](https://doi.org/10.1016/0040-1951(90)90188-E)
805 [1951\(90\)90188-E](https://doi.org/10.1016/0040-1951(90)90188-E).

806 Tindell, T., Watanabe, K., Imai, A., Takahashi, R., Boyce, A. J., Yonezu, K., Schersten,
807 A., Page, L., Ogata, T., 2018. The Kago low-sulfidation gold and silver deposit:
808 A peripheral mineralisation to the Nansatsu high-sulfidation system, southern
809 Kyushu, Japan. *Ore Geology Reviews* 102, 951-966.
810 <https://doi.org/10.1016/j.oregeorev.2017.10.027>.

811 Vennemann, T.W., Muntean, J.L., Kesler, S.E., O'Neil, J.R., Valley, J.W., Russell, N.,
812 1993. Stable isotope evidence for magmatic fluids in the Pueblo Viejo
813 epithermal acid sulfate Au-Ag deposit, Dominican Republic. *Economic*
814 *Geology* 88, 55-71. <https://doi.org/10.2113/gsecongeo.88.1.55>.

815 Vikre, P.G., 1989. Fluid-mineral relations in Comstock Lode. *Economic Geology* 84,
816 1574-1613. <https://doi.org/10.2113/gsecongeo.84.6.1574>.

817 Wang L., Qin, K-Z., Song, G.-x., and Li, G.-m., 2019. A review of intermediate
818 sulfidation epithermal deposits and subclassification. *Ore Geology Reviews*
819 107, 434-456. <https://doi.org/10.1016/j.oregeorev.2019.02.023>.

- 820 Waters, P.J., Cooke, D.R., Gonzales, R.I., Phillips, D., 2011. Porphyry and epithermal
821 deposits and $^{40}\text{Ar}/^{39}\text{Ar}$ geochronology of the Baguio district, Philippines.
822 *Economic Geology* 106, 1335–1363.
823 <http://doi.org/10.2113/econgeo.106.8.1335>.
- 824 White, N.C., and Hedenquist, J.W. (1995). Epithermal gold deposits: styles,
825 characteristics and exploration. *Society of Economic Geologists Newsletter* 23,
826 9-13.
- 827 Wilkinson, J.J., 2001. Fluid inclusions in hydrothermal ore deposits. *Lithos* 55, 229-
828 272. [https://doi.org/10.1016/S0024-4937\(00\)00047-5](https://doi.org/10.1016/S0024-4937(00)00047-5).
- 829 Yang, T.F., Lee, T., Chen, C-H., Cheng, S-N., Knittel, U., Punongbayan, R.S., Rasdas,
830 A.R., 1996. A double island arc between Taiwan and Luzon: consequence of
831 ridge subduction. *Tectonophysics* 258, 85-101. [https://doi.org/10.1016/0040-](https://doi.org/10.1016/0040-1951(95)00180-8)
832 [1951\(95\)00180-8](https://doi.org/10.1016/0040-1951(95)00180-8).
- 833 Zhang, C.-c., Sun, W.-d., Wang, J.-t., Zhang, L.-p., Sun, S.-j., Wu, K., 2017. Oxygen
834 fugacity and porphyry mineralization: A zircon perspective of Dexing porphyry
835 Cu deposit, China. *Geochimica et Cosmochimica Acta* 206, 343-363.
836 <https://doi.org/10.1016/j.gca.2017.03.013>.

837 **Figure captions**

838 **Figure 1.** Schematic map showing the features and structures in and surrounding the
839 Northern Luzon Segment, which forms part of the Taiwan-Luzon Arc as defined by
840 Yang et al. (1996). The segment is bounded to the east by the East Luzon Trough, and
841 to the west by the Manila Trench where an extinct mid-oceanic ridge (manifested by
842 the Scarborough Seamount Chain) of the South China Sea Basin is subducting. One of

843 the major structures traversing the segment is the Abra River Fault, a northern splay of
844 the Philippine Fault Zone (Aurelio, 2000).

845 **Figure 2.** a) Distribution of the known hydrothermal mineralization in the Mankayan
846 Mineral District (Chang et al., 2011; Manalo et al., 2018) and the surface projection of
847 the epithermal veins and small-scale tunnels of the Suyoc prospect. The location of the
848 Mankayan Mineral District is shown by the red dot on the inset map. b) Geology of the
849 district. Geology of the north and central part was modified from Garcia (1991) and
850 Sillitoe and Angeles (1985), whereas the southern part was derived from the data of
851 Itogon Suyoc Resources Incorporated. Exposures of the Apaoan Volcaniclastics are
852 located further north, and thus not included in this geologic map. Grey shades are the
853 projections of the location and extent of the mineralized areas in A.

854 **Figure 3.** Representative photos of the host rocks in Suyoc prospect: a) deformed
855 sequence of epiclastic sandstone of the Balili Formation; b) matrix-supported
856 conglomerate with clasts of aphanitic and porphyritic andesite of the Balili Formation;
857 c) thick beds of conglomerate of the Suyoc Conglomerate; d) silicified, matrix- to clast-
858 supported polymictic conglomerate of the Suyoc Conglomerate.

859 **Figure 4.** Representative photos of the vein-types and other mineralization features in
860 Suyoc: a) anastomosing quartz vein hosted in chloritized conglomerate inside the
861 Calixto tunnel; b) massive quartz-sulfide vein displaced by a fault (red dashed-line) in
862 argillized volcanoclastic rock at the Esperanza tunnel; c) quartz-carbonate vein
863 exhibiting weak crustiform texture with malachite and Fe-Mn oxide encrustations
864 cutting across a conglomerate with surficial cover of limonite at the Elizabeth tunnel;
865 d) quartz-carbonate vein cutting the quartz vein at the Elizabeth tunnel; e) gypsum veins

866 hosted in conglomerate inside the Manuit tunnel; and f) an outcrop of massive gypsum
867 and pyrite in conglomerate. Veins are outlined by white dashed lines.

868 **Figure 5.** Hand specimen of the three major vein-types: a) quartz vein consisting of
869 angular to sub-angular quartz and wall rock fragments exhibiting cockade texture, b)
870 quartz-sulfide vein characterized by vuggy quartz and pyrite-chalcopyrite exhibiting
871 massive texture; c) quartz-carbonate vein displaying asymmetrical crustiform texture
872 characterized by outer quartz and inner colloform to macrocrystalline rhodochrosite (qz
873 = quartz; rds = rhodochrosite; py = pyrite; ccp = chalcopyrite; cry = cryptocrystalline;
874 mac = macrocrystalline).

875 **Figure 6.** Representative photomicrographs of the different veins: a) silicified wall
876 rock fragment bounded by microcrystalline quartz; b) prismatic quartz exhibiting comb
877 texture interlayered with massive microcrystalline quartz; c) micro- to macrocrystalline
878 quartz displaying massive texture with associated sulfides; d) interlayered massive
879 quartz and cryptocrystalline to macrocrystalline rhodochrosite; e) fractured euhedral to
880 subhedral pyrite crystals with chalcopyrite infill intergrown with sphalerite; f)
881 interlocking pyrite, chalcopyrite, galena, and sphalerite that exhibits chalcopyrite
882 disease; g) galena with minute inclusions of bournonite; and h) electrum encapsulated
883 within a euhedral pyrite crystal. (a-d in cross-polarized transmitted light and e-h in
884 plane-polarized reflected light; qz = quartz; rds = rhodochrosite; SWF = silicified wall
885 rock fragment; py = pyrite; ccp = chalcopyrite; sp = sphalerite; gn = galena; bno =
886 bournonite; el = electrum; Au = Au-bearing mineral).

887 **Figure 7.** Backscatter electron images of the three analyzed Au-bearing minerals in
888 pyrite from the quartz-carbonate vein. Red circles are the analysis points. Photos a, b
889 and c contain the Au-bearing minerals 1, 2 and 3, respectively. (py = pyrite; gn = galena)

890 **Figure 8.** Backscatter electron images of the three sphalerite crystals in quartz-
891 carbonate vein analyzed for FeS composition and their corresponding FeS mole %
892 diagrams. Photos a, b and c contain sphalerite 1, 2 and 3, respectively. Red circles are
893 the analysis points. (py = pyrite; ccp = chalcopyrite; sp = sphalerite; gn = galena)

894 **Figure 9.** (a-b) Representative photomicrographs of quartz-hosted fluid-inclusions
895 from the quartz vein (photo a) and the quartz-carbonate vein (photo b). Legend: L:
896 liquid phase, V: vapor phase. (c-e) Scatterplot of homogenization temperature versus
897 salinity from quartz-hosted primary fluid inclusions is shown in diagram c for quartz
898 vein, diagram d for quartz-sulfide vein, and diagram e for quartz-carbonate vein. The
899 x- and y-axis have corresponding histograms to show their modal values. The dashed
900 arrow represents the inferred trend of the values.

901 **Figure 10.** X-ray diffractograms from bulk and oriented analysis of the altered wall
902 rocks adjacent to the three major vein-types. (chl = chlorite; kln = kaolinite; cly = clay;
903 qz = quartz; cal = calcite; py = pyrite; ill = illite)

904 **Figure 11.** Sulfur fugacity ($\log f_{S_2}$) versus temperature ($1000/T$) diagram showing the
905 different sulfidation states, with their corresponding sulfide assemblages from Einaudi
906 et al. (2003), and FeS mole percent lines from Barton and Toulmin (1966). The red bar
907 shows the projected sulfidation state of Suyoc prospect's quartz-carbonate vein plotted
908 using the values of modal homogenization temperature (240-250°C) in quartz (x-axis)
909 and FeS mole percent (0.51-8.30) values from sphalerite crystals coexisting with pyrite
910 (gray dashed lines). (cv = covellite, dg = digenite, py = pyrite, bn = bornite, ccp =
911 chalcopyrite, po = pyrrhotite, asp = arsenopyrite, lo = loellingite)

912 **Figure 12.** List of the common alteration minerals found in epithermal deposits from
913 the compilation of White and Hedenquist (1995). Highlighted in red are the alteration

914 minerals present in the altered wall rocks of the three major vein-types of the Suyoc
915 prospect.

916 **Figure 13.** $\delta^{34}\text{S}$ versus temperature ($^{\circ}\text{C}$) diagram showing the sulfide $\delta^{34}\text{S}$
917 compositional evolution through oxidized and reduced cooling pathway from a source
918 with $\sim 5\text{‰}$ bulk sulfur isotope composition ($\delta^{34}\text{S}_{\Sigma\text{S}}$). The oxidized and reduced $\delta^{34}\text{S}$
919 composition paths were estimated for $+5\text{‰}$ $\delta^{34}\text{S}_{\Sigma\text{S}}$ using the $\delta_{\text{sulfate}} - \delta_{\text{sulfide}}$ diagram of
920 Rye (2005). The $+5\text{‰}$ represents the bulk composition for the mineralization in the
921 Mankayan Mineral District based on Imai (2000) and Manalo et al. (2018). Plotted
922 within these oxidized and reduced fields are the sulfide $\delta^{34}\text{S}$ values and corresponding
923 homogenization temperature of the quartz-sulfide vein and quartz-carbonate vein of the
924 Suyoc prospect.

925 **Figure 14.** a) δD composition of the two distinct liquids produced from the causative
926 magma of the Far Southeast porphyry Cu system during its evolution (adapted from
927 Shinohara and Hedenquist, 1997). In the early stage, in which $\sim 30\%$ of the magma is
928 crystallized and magma convection is taking place, single-phase, high temperature
929 liquid with δD of about -25‰ was discharged from the melt as a result of open system
930 degassing. In the later stage, in which $\sim 50\%$ of the magma is crystallized, with magma
931 convection and degassing being halted, single-phase, low temperature liquid with δD
932 of about -40‰ is discharged from the melt. b) $\delta\text{D}_{\text{water}}$ vs $\delta^{18}\text{O}_{\text{water}}$ diagram showing
933 the meteoric water mixing trend of advanced argillic alteration and sericitic alteration
934 of the Far Southeast (FSE) porphyry Cu-Au deposit that represent the vapor and late
935 low temperature liquid (LLTL), respectively (Hedenquist et al., 1998). Plotted values
936 and their corresponding references is shown in Table 5. Magmatic water compositions
937 were defined by Taylor (1992). Volcanic waters were derived from Giggenbach (1992).

938 **Figure 15.** An illustration depicting the potential presence of porphyry Cu and high
939 sulfidation (HS) epithermal mineralization cogenetic with the actual intermediate
940 sulfidation epithermal (ISE) veins of the Suyoc prospect. This interpretation is based
941 on the widely accepted idea about porphyry-epithermal association (Hedenquist et al.,
942 1998; Sillitoe and Hedenquist, 2003; Chang et al., 2011; Wang et al., 2019). This
943 particular illustration is derived from the model of Sillitoe (2010) for a typical
944 porphyry-epithermal system.

945 **Figure 16.** Map showing a proposed prospective area in the vicinity (~1km radius) of
946 the intermediate sulfidation epithermal (ISE) veins of the Suyoc prospect. This
947 proposed radius follows the spatial configuration of the Victoria ISE deposit with the
948 Far Southeast porphyry Cu-Au deposit and the Lepanto high sulfidation epithermal
949 (HSE) deposit (Chang et al., 2011). Also included are the locations of other known
950 prospects and deposits in the district, as well as the distribution of mapped lithocaps
951 based on Chang et al. (2011).

952 **Table Captions**

953 **Table 1a.** Elemental composition of Au-bearing minerals in the quartz-carbonate vein.

954 **Table 1b.** Elemental composition of sphalerite crystals coexisting with pyrite in the
955 quartz-carbonate vein. The calculated FeS mole % is included.

956 **Table 2.** Homogenization temperature (T_h) and final-ice melting temperature (T_{fim})
957 acquired from microthermometry of primary fluid inclusions from each vein-type.
958 Salinity was calculated from T_{fim} using the formula of Bodnar (1993).

959 **Table 3.** δD from the fluid inclusion in quartz and $\delta^{18}O$ values from the quartz of the
960 three major vein-types. $\delta^{18}O$ values in equilibrium with water ($\delta^{18}O_{water}$) were
961 calculated via the equation provided by Clayton et al. (1972) for 200-500°C quartz-

962 water system. The temperatures used for the equation were taken from obtained modal
963 homogenization temperature (T_h) values.

964 **Table 4.** Summary of the characteristics of the three major vein-types of the Suyoc
965 prospect. (qz = quartz, rds = rhodochrosite, py = pyrite, ccp = chalcopyrite, sp =
966 sphalerite, gn = galena, Au/Ag = native gold and electrum, bno = bournonite)

967 **Table 5.** Mean temperature, δD_{water} and $\delta^{18}O_{\text{water}}$ data of the Suyoc prospect, Antamok
968 and Acupan intermediate sulfidation epithermal deposits and the meteoric water in
969 Baguio-Mankayan (~500-1500 masl). Data from the Far Southeast porphyry Cu-Au
970 deposit include compositions of advanced argillic alteration from alunite, and average
971 compositions of potassic alteration from biotite and sericitic alteration from illite.
972 (LLTL = late low temperature liquid). References: 1 = Hedenquist et al. (1998); 2 =
973 Sawkins et al. (1979); 3 = JICA (1984)

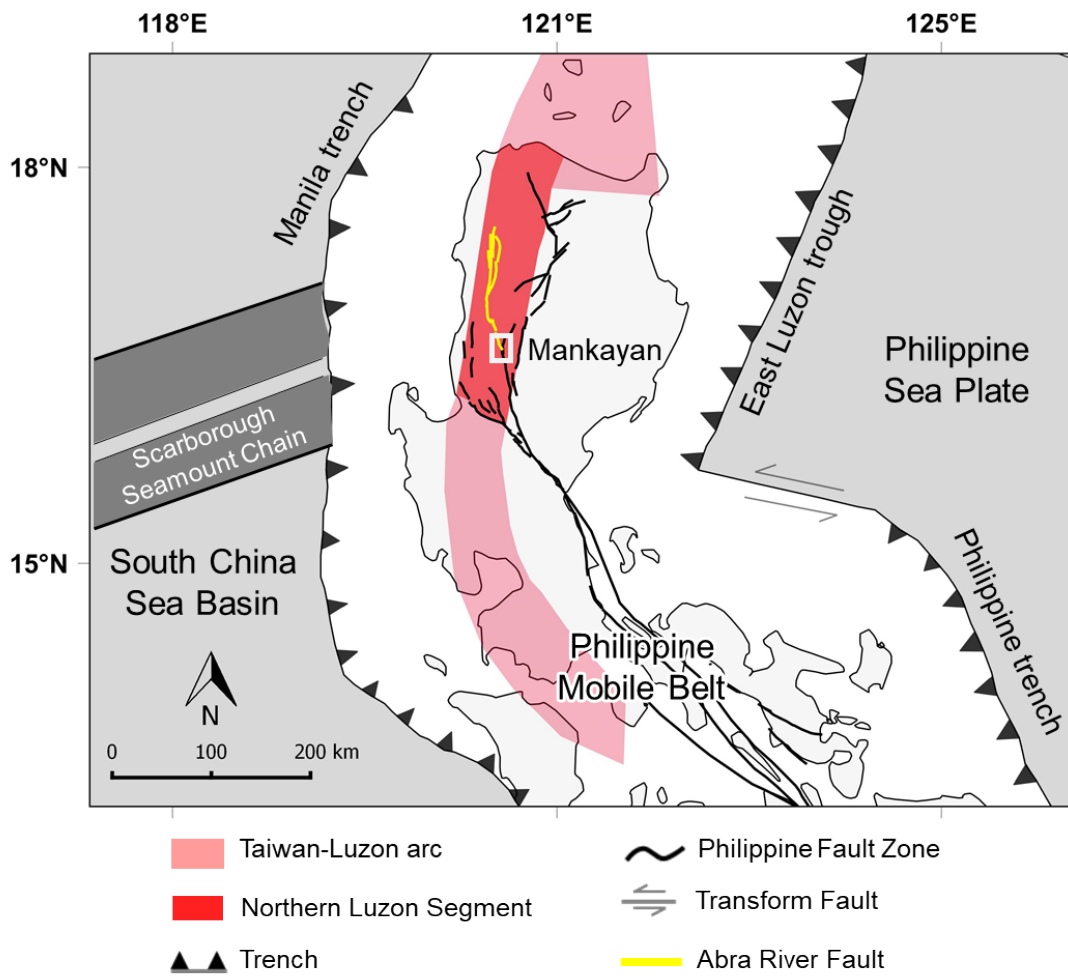


Figure 1.

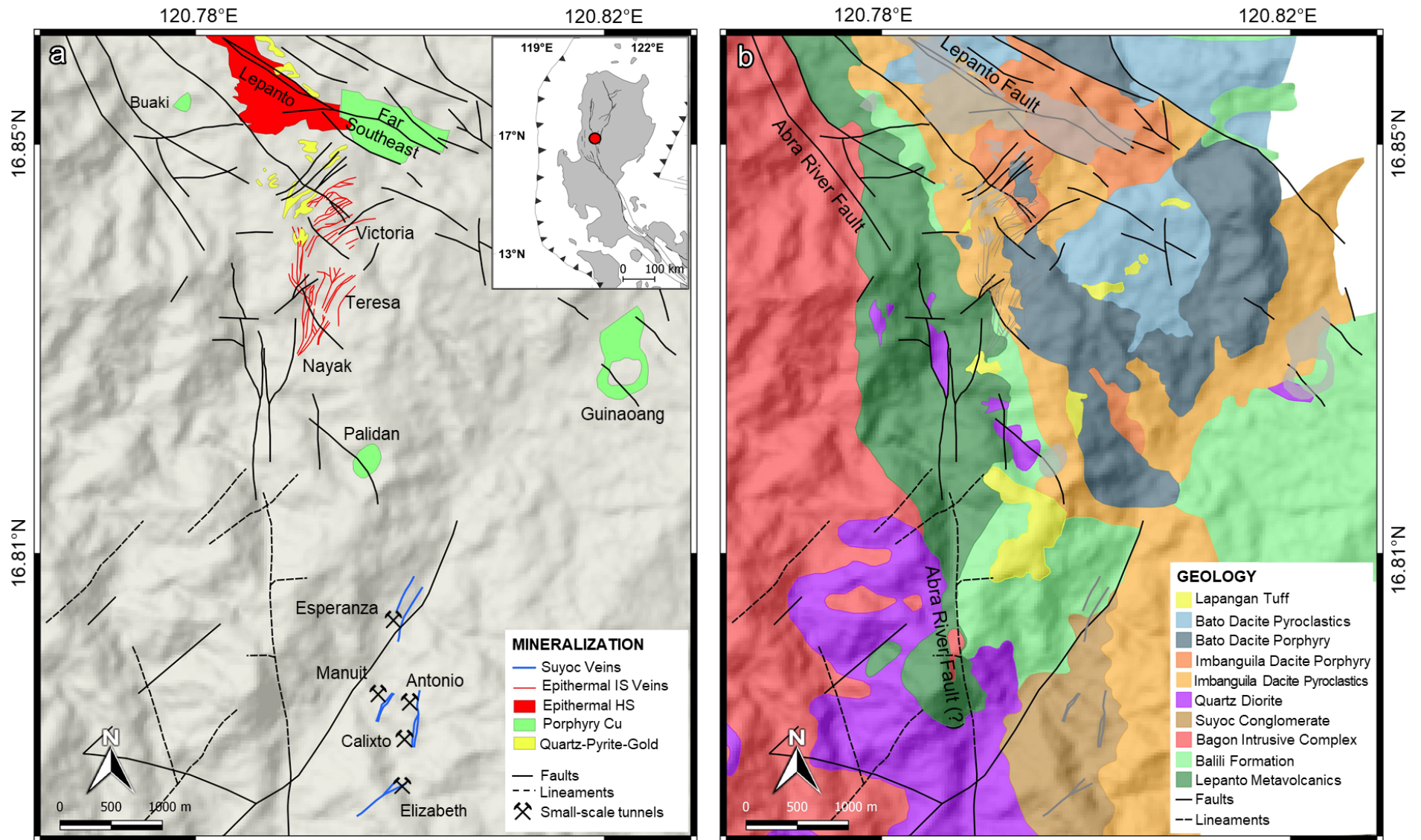


Figure 2.

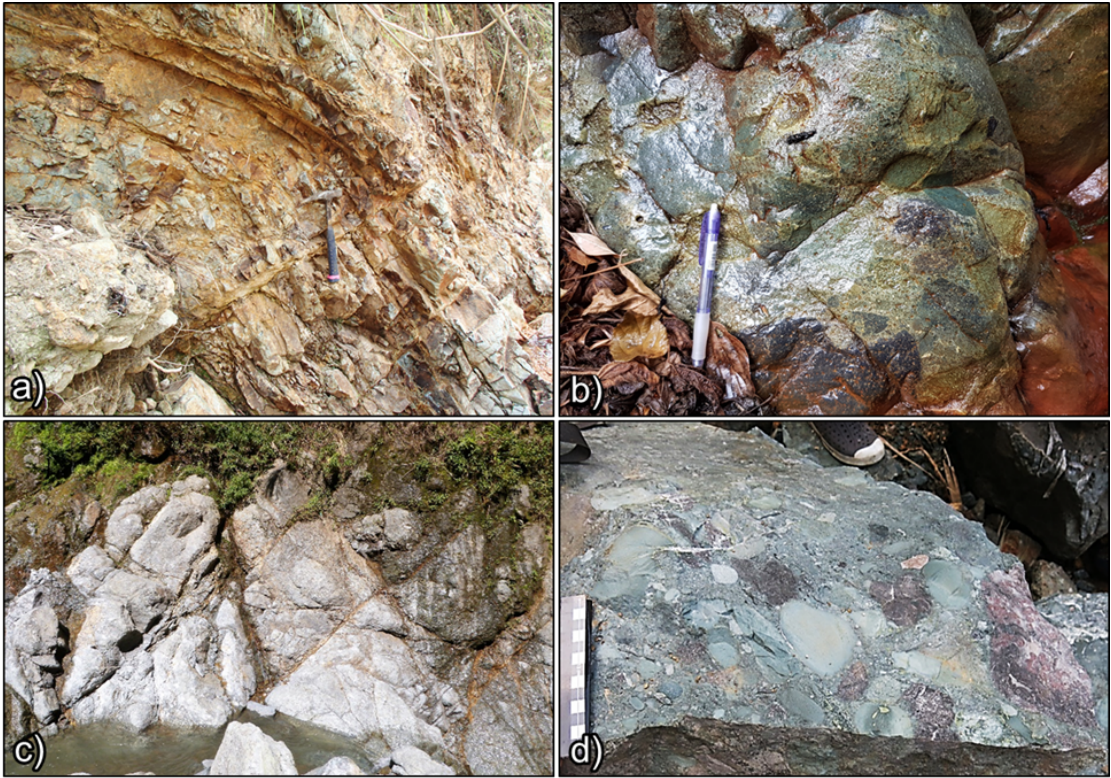


Figure 3.

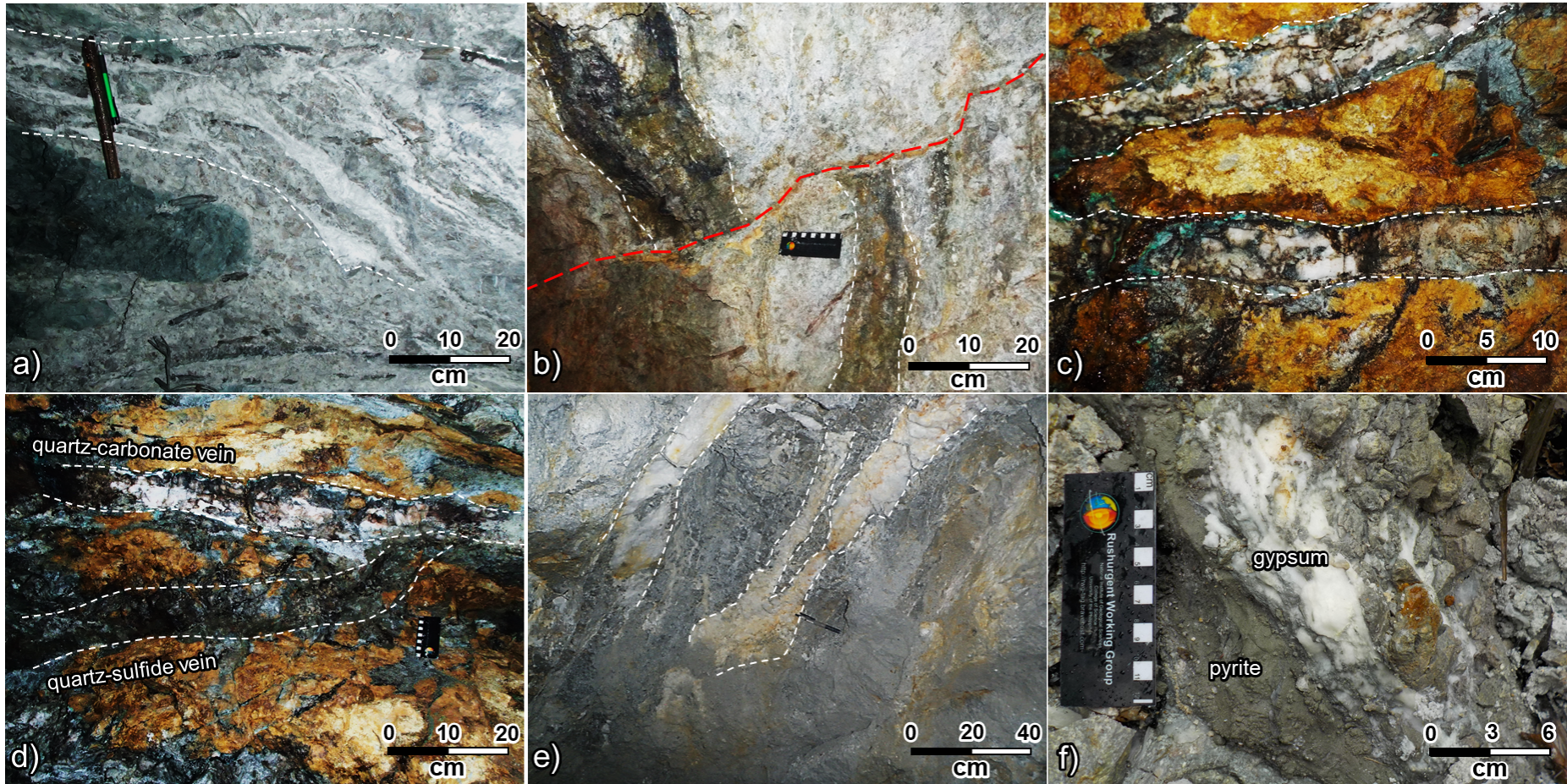


Figure 4.

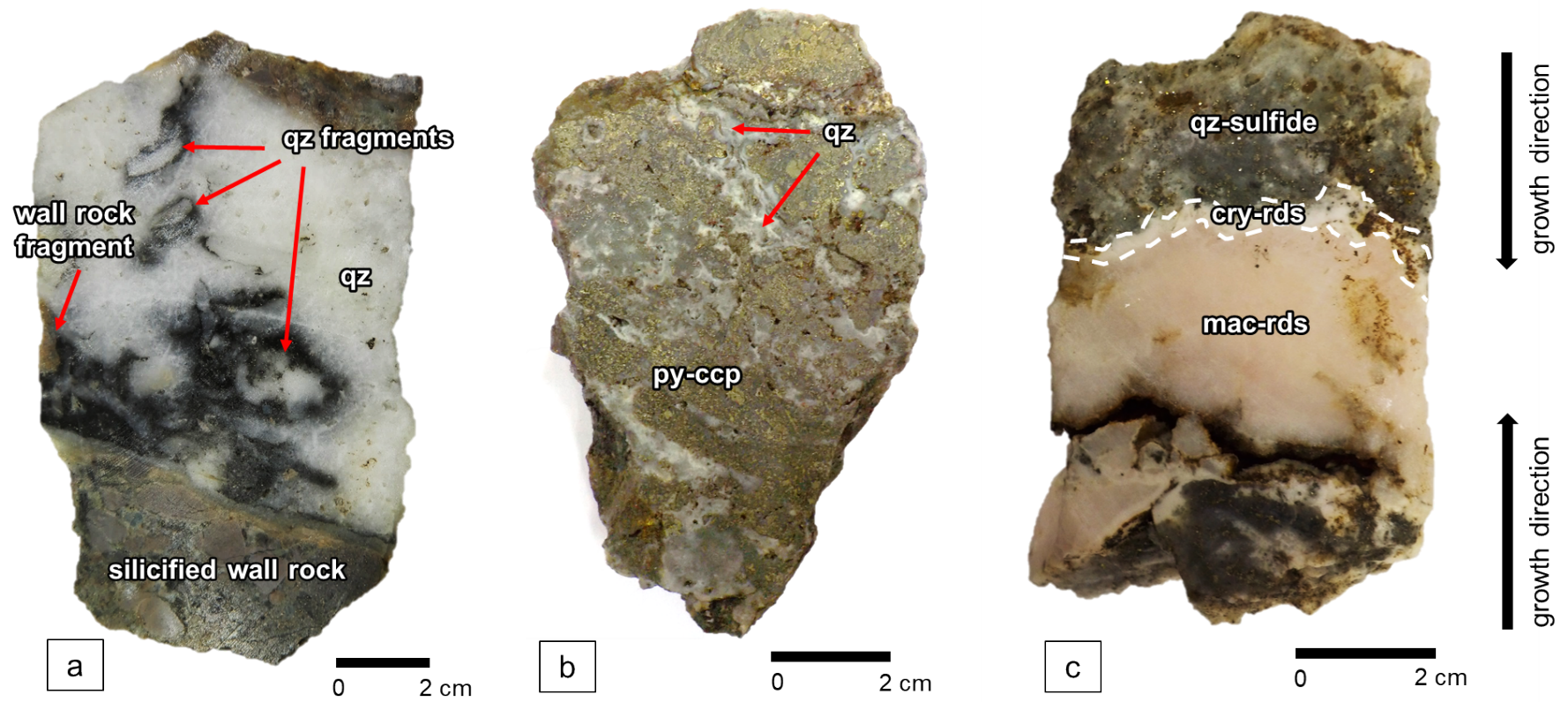


Figure 5.

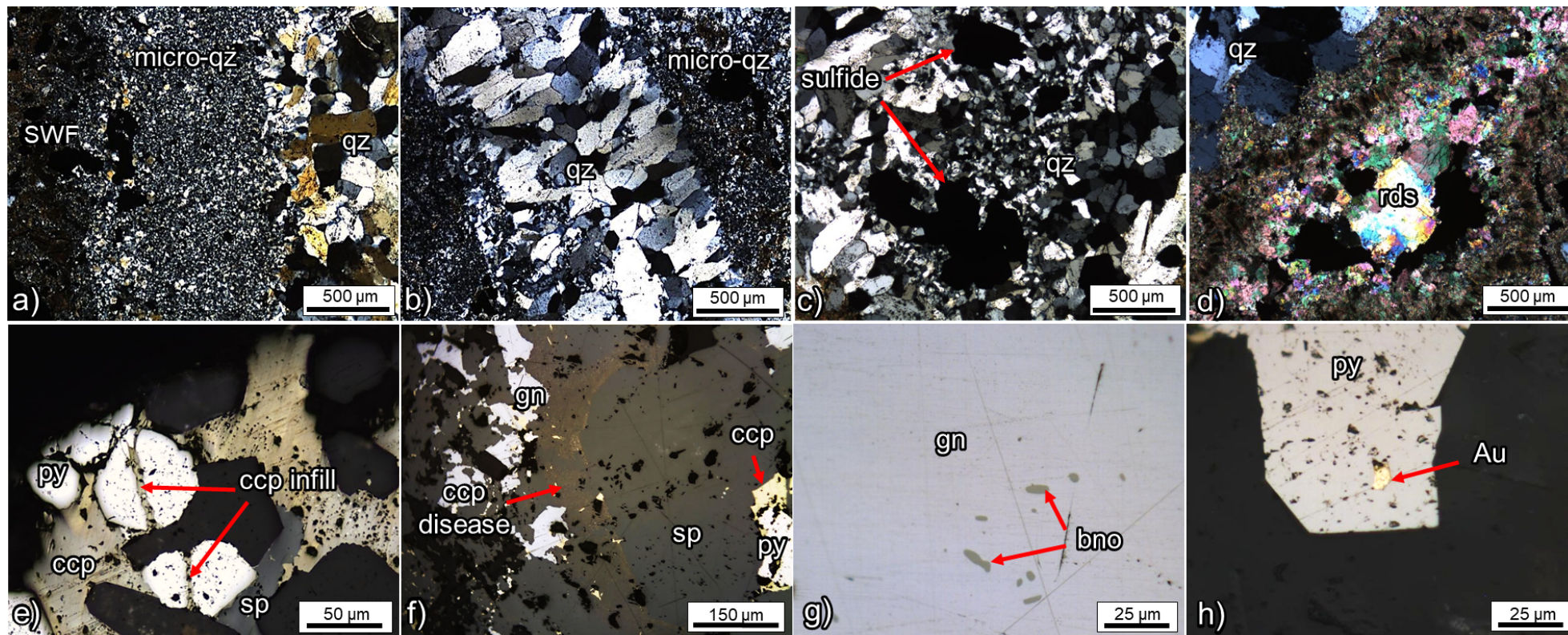


Figure 6.

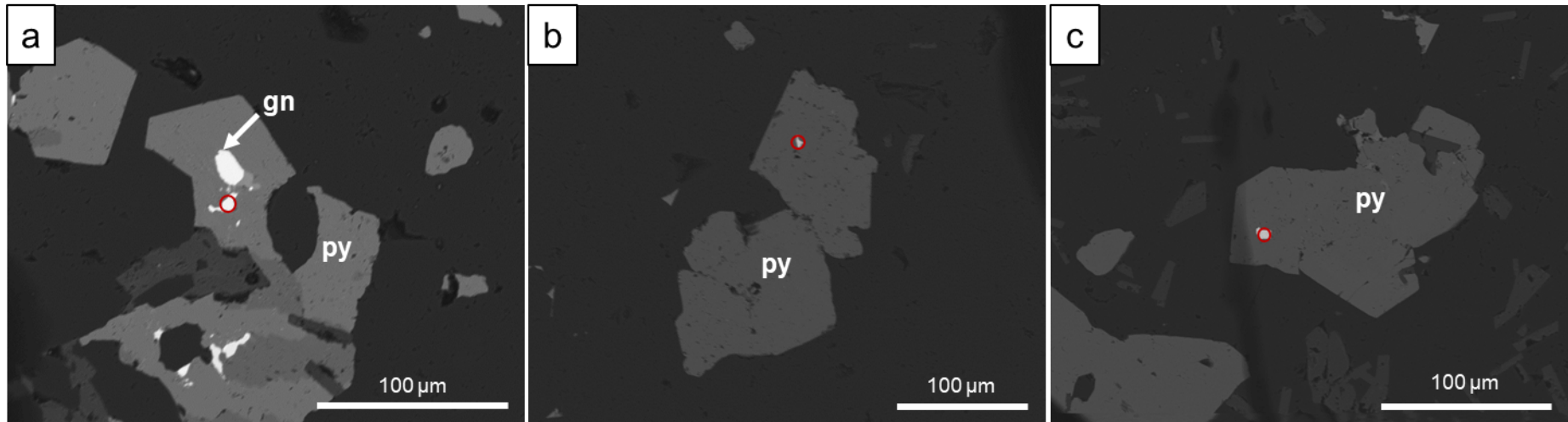


Figure 7.

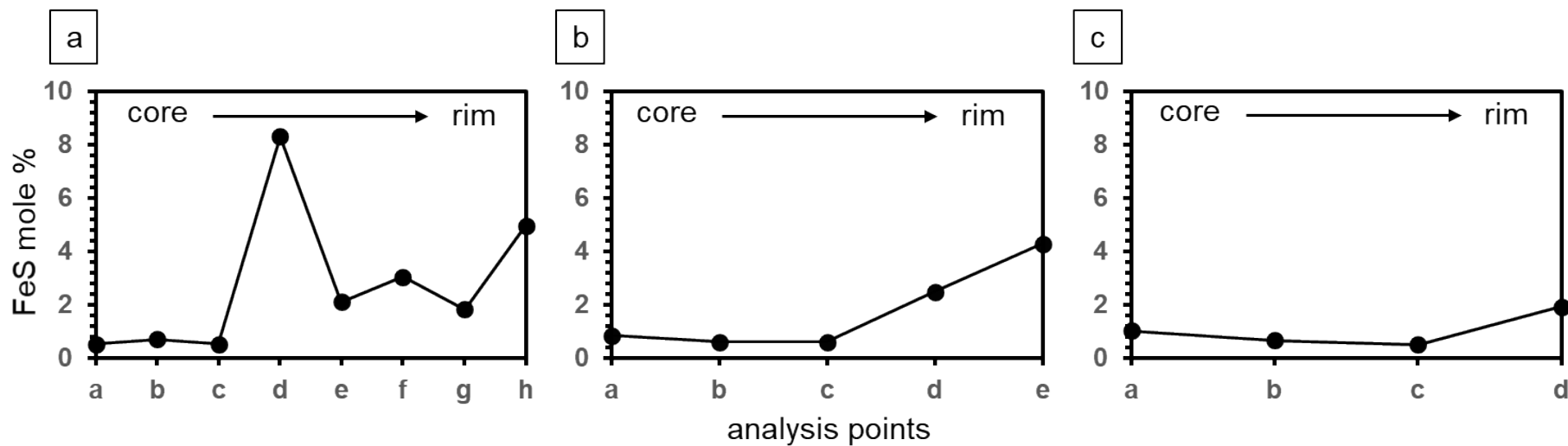
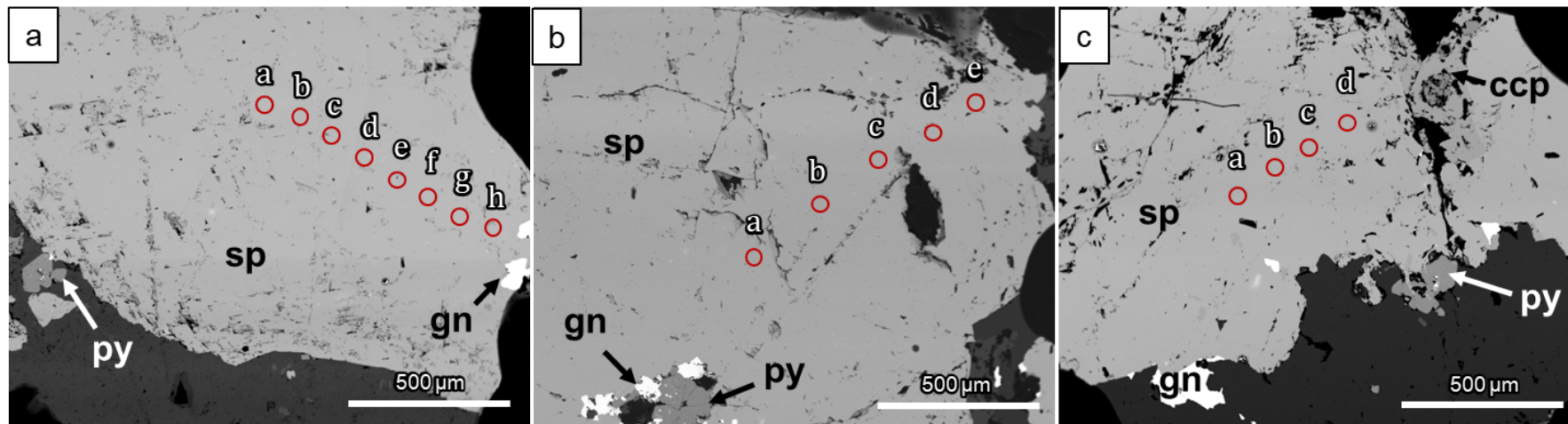


Figure 8.

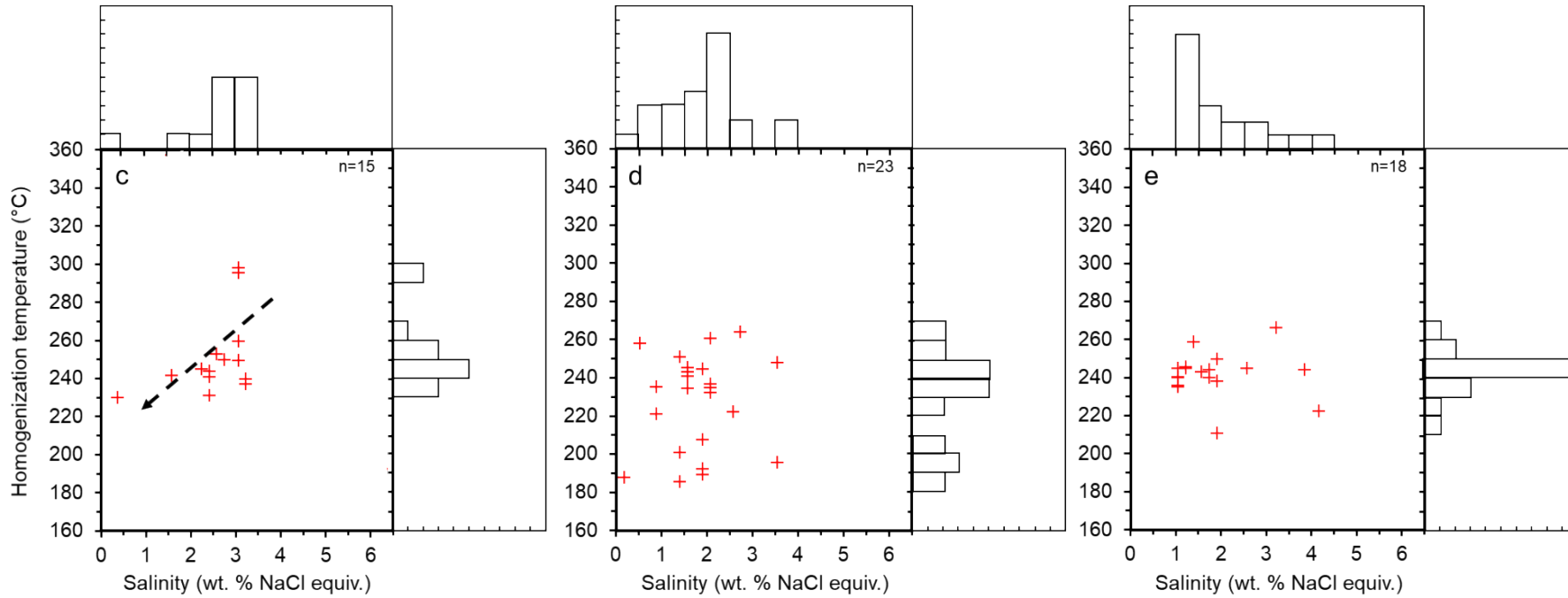
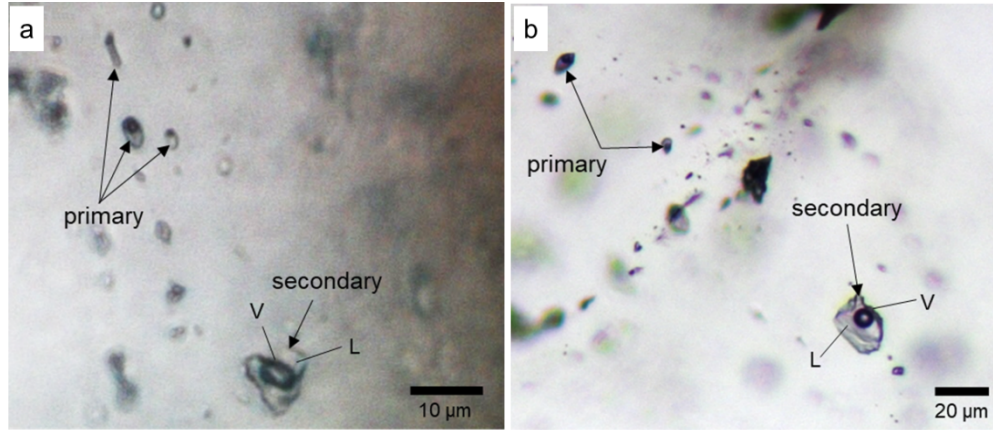


Figure 9.

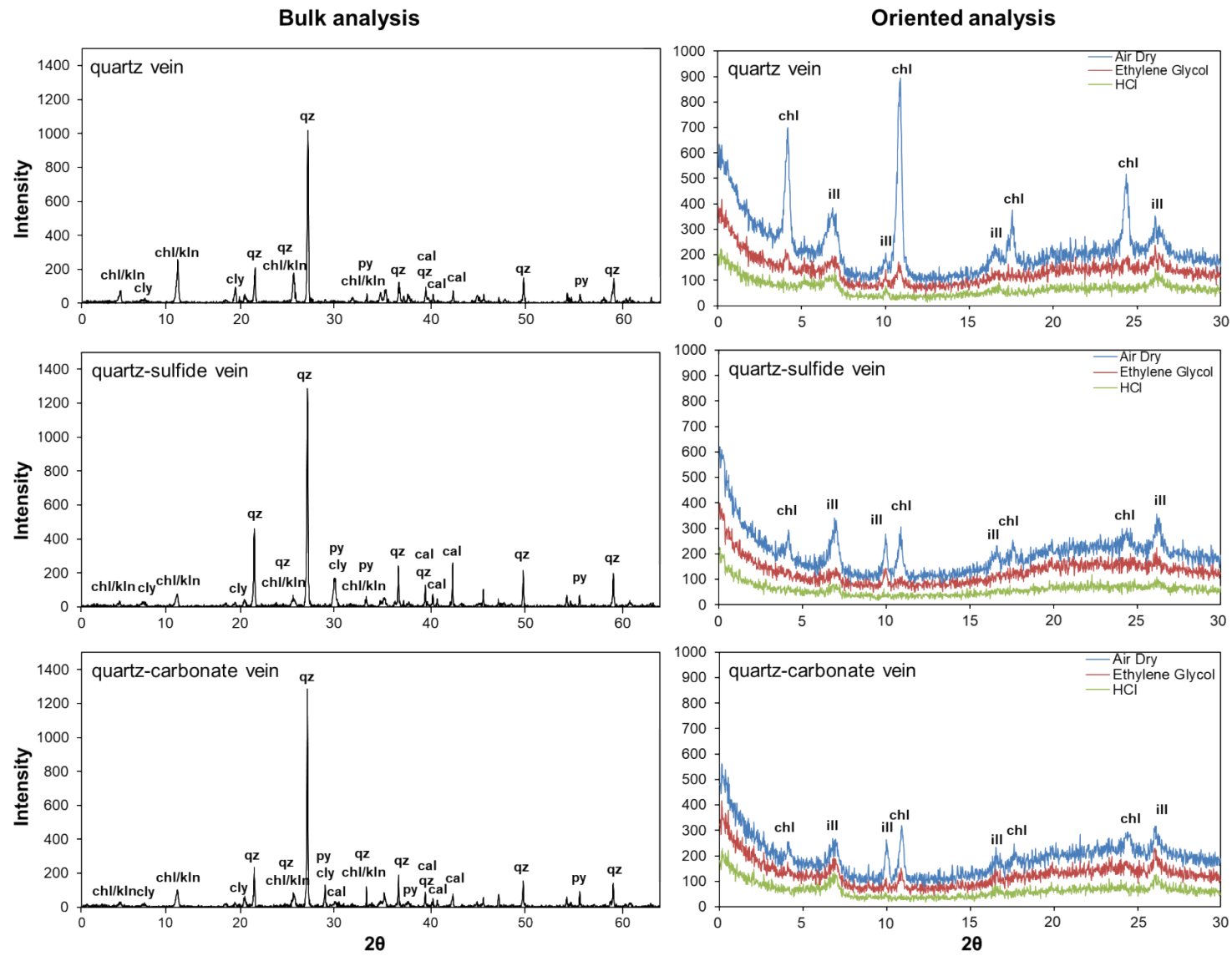


Figure 10.

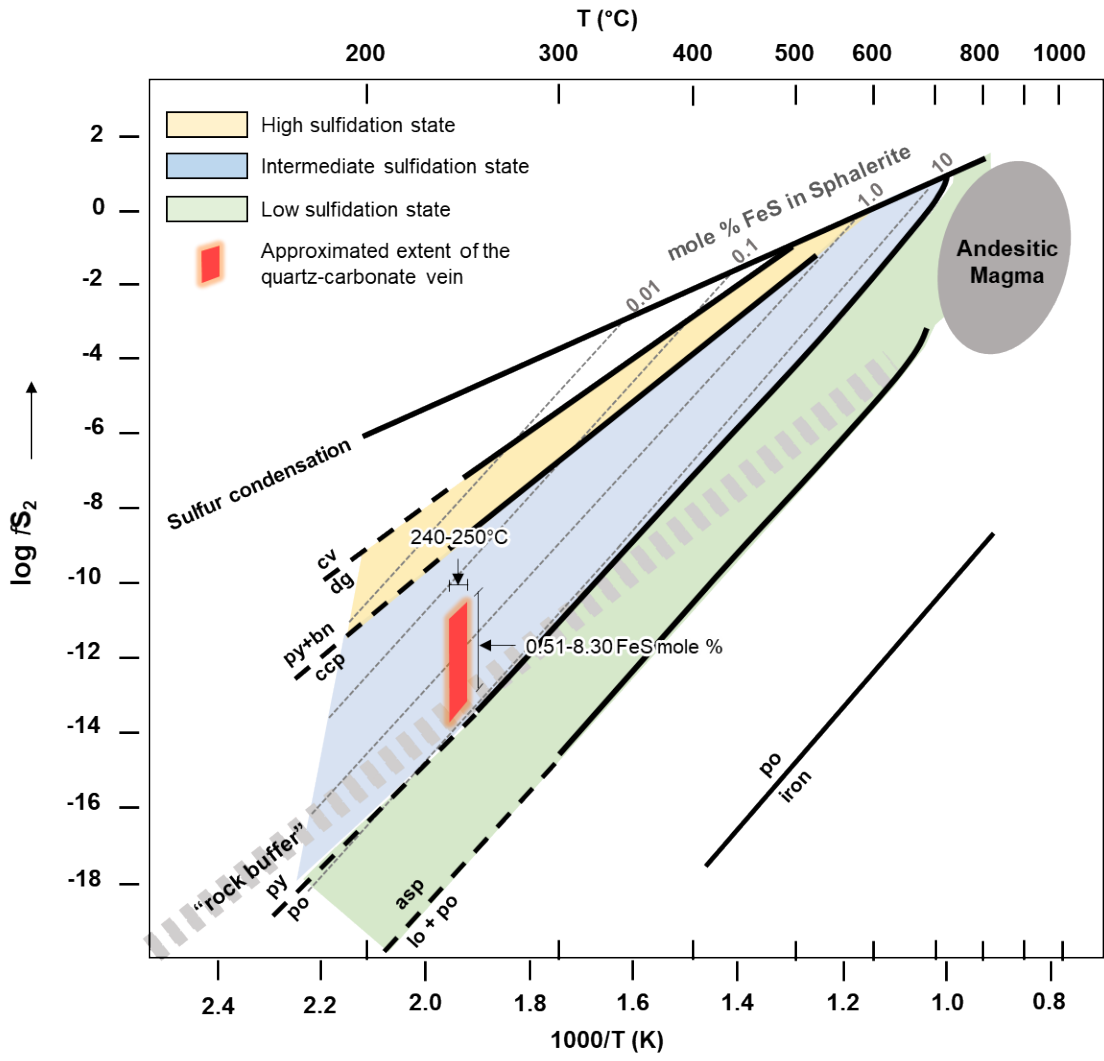


Figure 11.

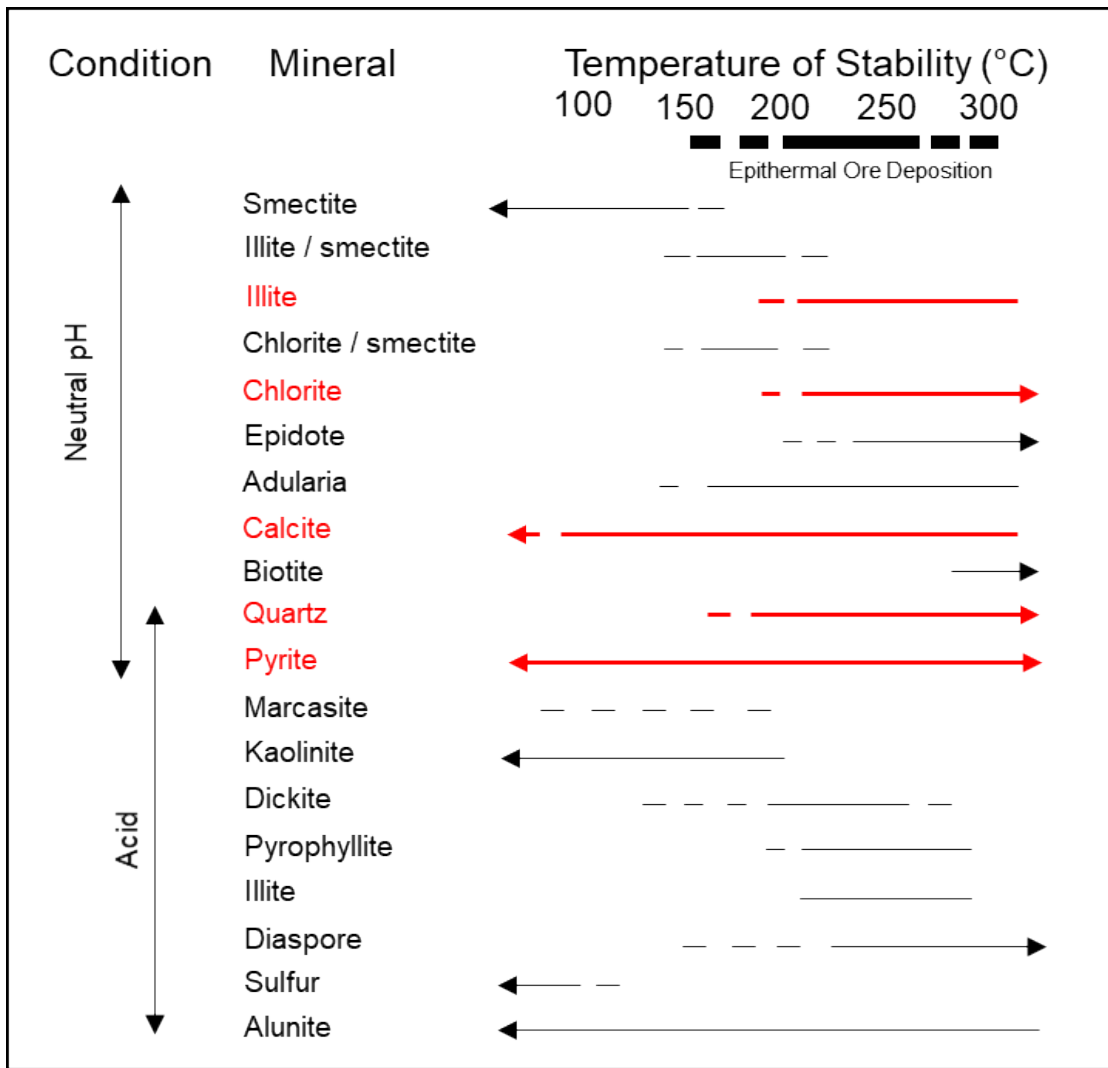


Figure 12.

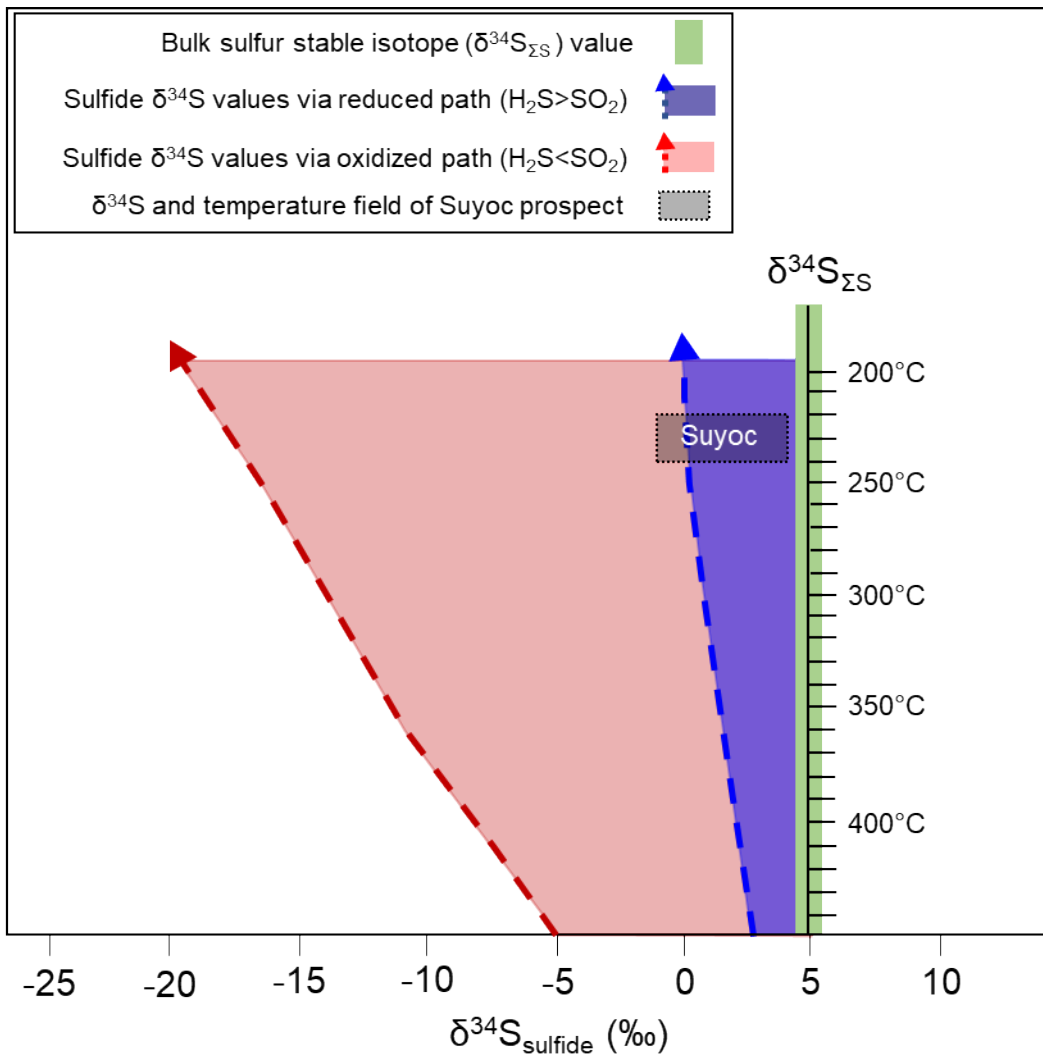


Figure 13.

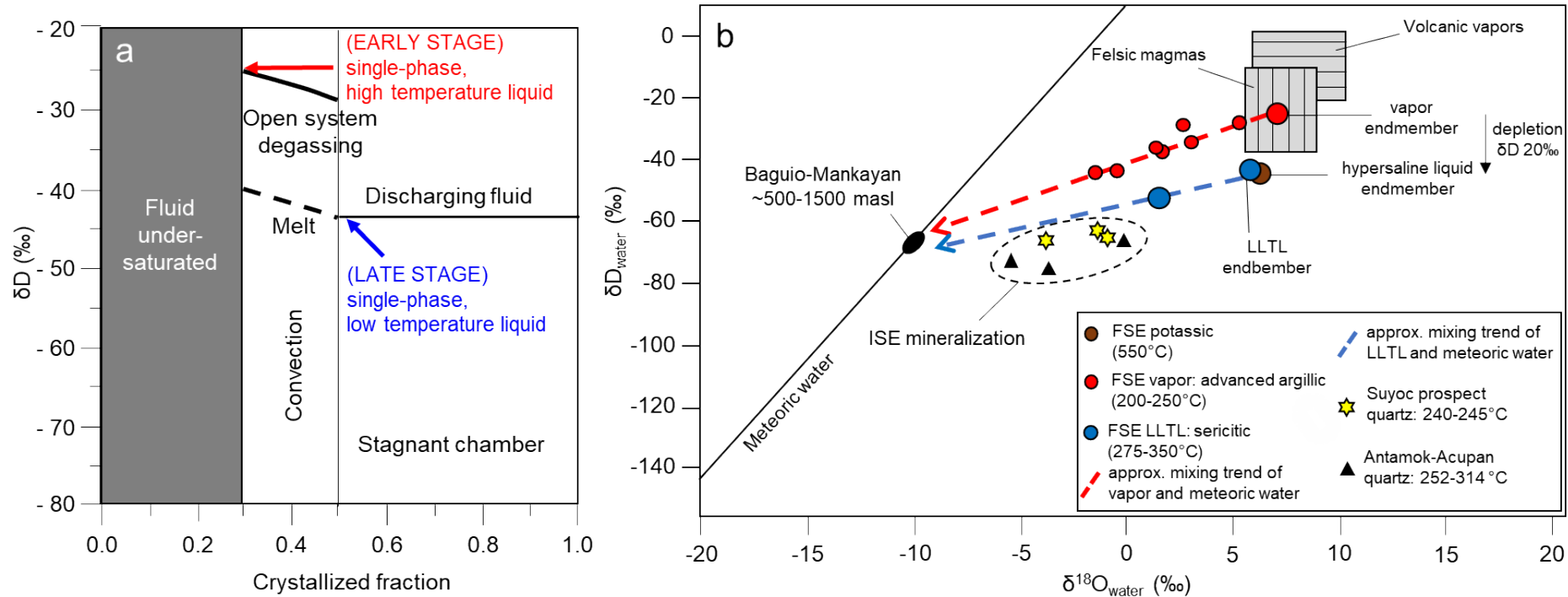


Figure 14.

Southern Mankayan Mineral District

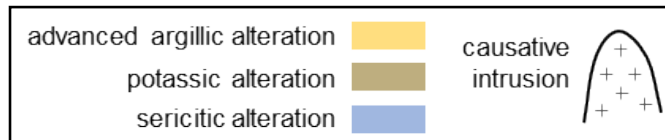
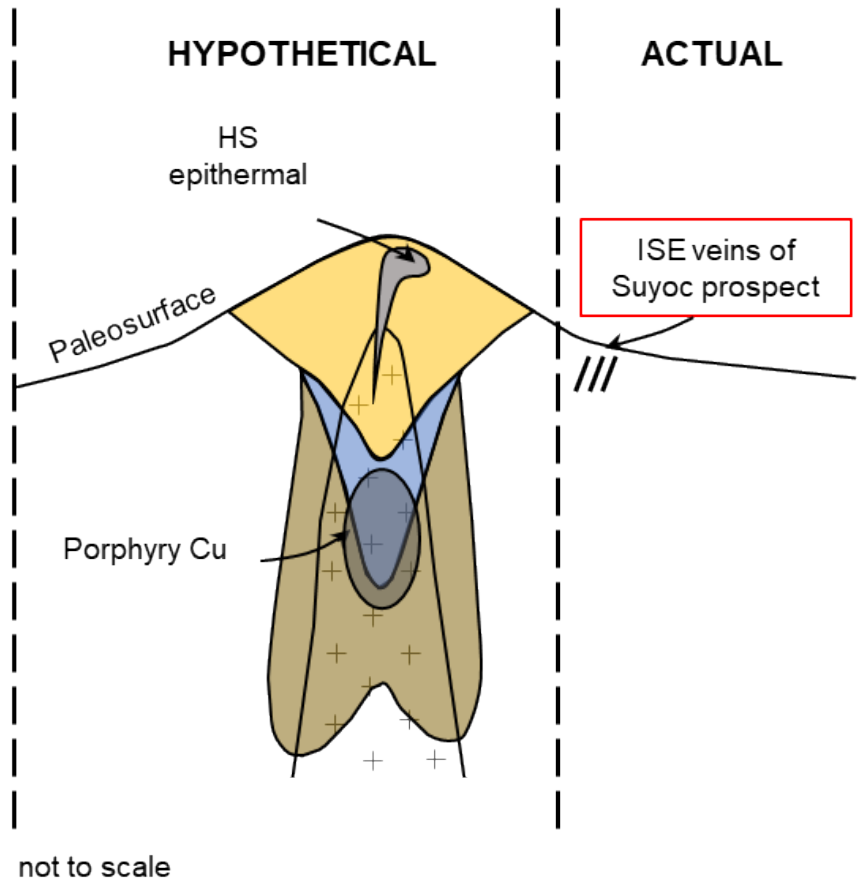


Figure 15.

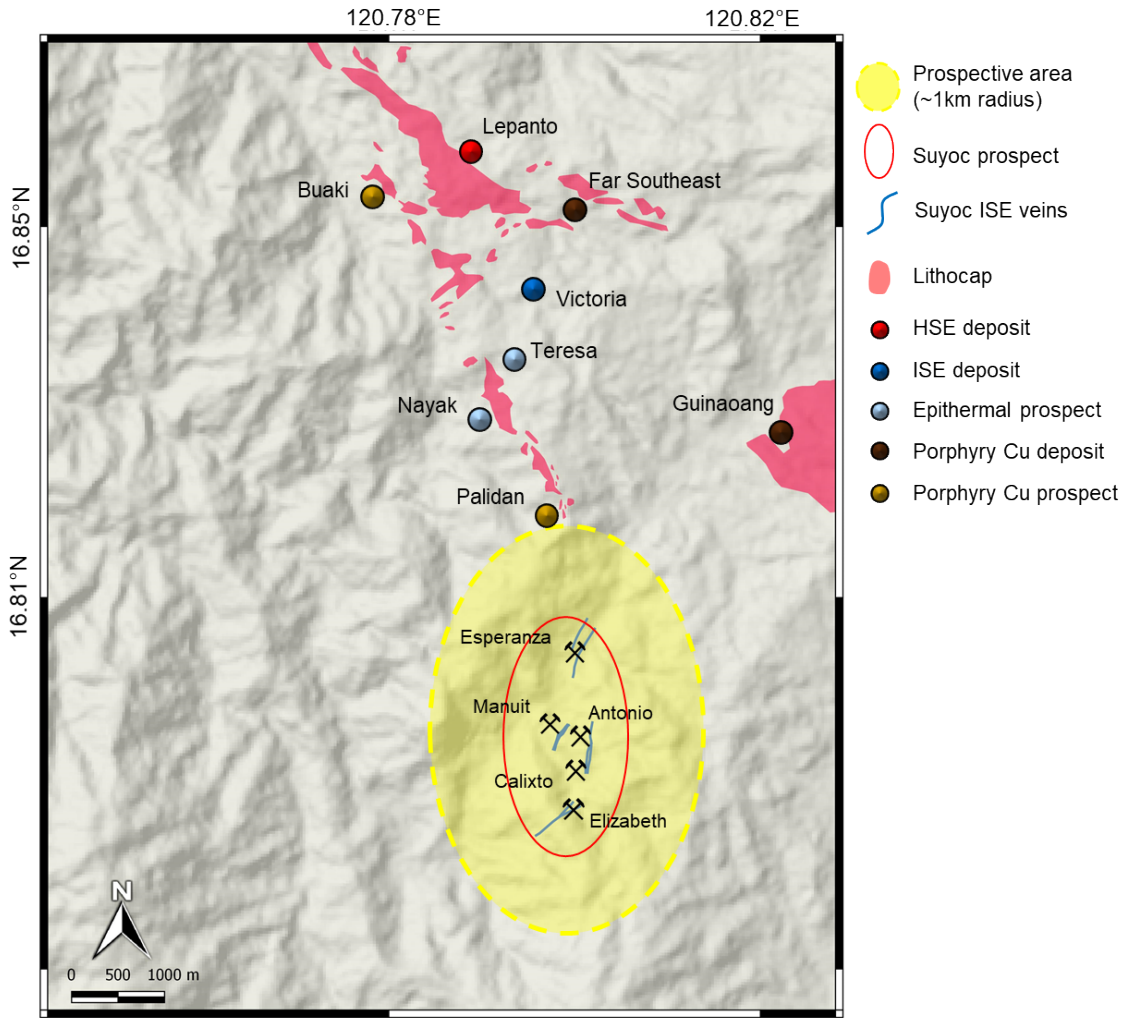


Figure 16.

Table 1a.

Au-bearing mineral	Elemental composition (mass %)		
	Au	Ag	TOTAL
1	73.53	27.66	101.19
2	63.10	37.28	100.38
3	83.24	18.58	101.82

Table 1b.

	Elemental composition (mass %)			TOTAL	FeS mole %	
	Zn	Fe	S			
sphalerite 1 ↑ ↓	core	65.31	0.35	31.56	97.23	0.53
		64.62	0.46	32.10	97.17	0.71
		64.82	0.34	31.65	96.81	0.52
		58.87	5.33	32.79	96.99	8.30
		64.10	1.37	31.63	97.10	2.09
		62.70	1.97	32.51	97.18	3.04
	rim	64.32	1.18	31.67	97.17	1.81
sphalerite 2 ↑ ↓	core	62.10	3.24	31.81	97.15	4.95
		64.69	0.56	31.34	96.59	0.85
		64.77	0.40	31.86	97.02	0.61
		64.97	0.40	31.96	97.33	0.61
	rim	63.54	1.61	32.19	97.34	2.48
sphalerite 3 ↑ ↓	core	61.89	2.77	32.16	96.81	4.28
		65.15	0.67	31.70	97.53	1.02
		64.86	0.43	31.55	96.84	0.66
	rim	65.40	0.34	31.53	97.27	0.51
	64.11	1.25	31.11	96.47	1.91	

Table 2.

No.	Quartz vein			Quartz-sulfide vein			Quartz-carbonate vein		
	T _h (°C)	T _{fm} (°C)	Salinity (wt. % NaCl equiv.)	T _h (°C)	T _{fm} (°C)	Salinity (wt. % NaCl equiv.)	T _h °C	T _{fm} °C	Salinity (wt. % NaCl equiv.)
1	230.2	-0.2	0.4	258.0	-0.3	0.5	211.0	-1.1	1.9
2	240.0	-1.9	3.2	189.3	-1.1	1.9	249.9	-1.1	1.9
3	202.0	-1.2	2.1	251.0	-0.8	1.4	245.0	-0.6	1.1
4	253.0	-1.5	2.6	221.2	-0.5	0.9	258.9	-0.8	1.4
5	250.0	-1.6	2.7	188.0	-0.1	0.2	245.0	-0.7	1.2
6	298.1	-1.8	3.1	235.3	-0.5	0.9	243.0	-0.9	1.6
7	295.5	-1.8	3.1	185.5	-0.8	1.4	245.5	-0.7	1.2
8	259.7	-1.8	3.1	264.2	-1.6	2.7	240.1	-1.0	1.7
9	249.5	-1.8	3.1	245.6	-0.9	1.6	244.0	-1.0	1.7
10	241.6	-0.9	1.6	222.4	-1.5	2.6	235.3	-0.6	1.1
11	245.2	-1.3	2.2	260.6	-1.2	2.1	240.5	-0.6	1.1
12	243.9	-1.4	2.4	248.0	-2.1	3.5	240.0	-0.6	1.1
13	231.3	-1.4	2.4	236.7	-1.2	2.1	244.3	-2.3	3.9
14	237.2	-1.9	3.2	195.9	-2.1	3.5	238.1	-1.1	1.9
15	241.0	-1.4	2.4	232.2	-1.2	2.1	236.0	-0.6	1.1
16				234.9	-1.2	2.1	245.1	-1.5	2.6
17				207.8	-1.1	1.9	222.3	-2.5	4.2
18				192.5	-1.1	1.9	266.2	-1.9	3.2
19				234.5	-0.9	1.6			
20				243.1	-0.9	1.6			
21				240.8	-0.9	1.6			
22				244.6	-1.1	1.9			
23				201.00	-0.80	1.40			

Table 3.

Vein-type	$\delta D_{\text{fluid inclusion}}$ (‰)	$\delta^{18}O_{\text{quartz}}$ (‰)	Modal T_h (°C)	$\delta^{18}O_{\text{water}}$ (‰)	$\delta^{34}S_{\text{pyrite}}$ (‰)
quartz	-65	8.7	240 - 250	-0.7 to -0.2	
		7.5		-1.9 to -1.4	
quartz-sulfide	-66	5.6	230 - 250	-4.4 to -3.4	-1.1
		5.5		-4.4 to -3.4	-0.1
quartz-carbonate	-63	7.8	240 - 250	-1.6 to -1.2	3.9
		7.7		-1.7 to -1.2	3.8

Table 4.

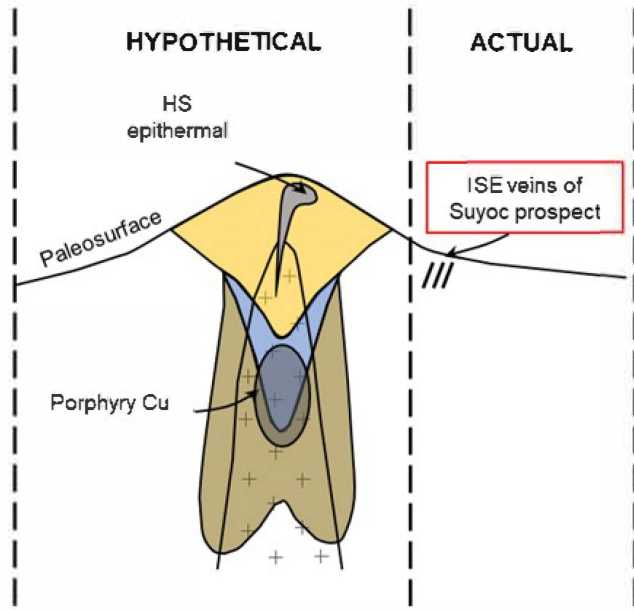
Characteristics	quartz vein	quartz-sulfide vein	quartz-carbonate vein
Mineralogy	qz+py+ccp	qz+py+ccp+sp	qz+rds+ccp+sp+gn+Au/Ag±bno
Texture	massive, cockade	massive, comb	massive, crustiform
Fluid inclusion variety	liquid-rich dominated	liquid-rich dominated	liquid-rich dominated
Homogenization temperature (°C)	240-250	230-250	240-250
Salinity (wt. % NaCl eq.)	2.5-3.5	2.0-2.5	1.0-1.5
Alteration	illite, chlorite, pyrite, quartz	illite, chlorite, pyrite, quartz, calcite	illite, chlorite, pyrite, quartz, calcite

Table 5.

	Mineral/Alteration	Temp. (°C)	δD_{water} (‰)	$\delta^{18}O_{\text{water}}$ (‰)	Reference	
Suyoc	quartz	245	-65	-1.1		• The Suyoc vein prospect displays typical intermediate sulfidation epithermal signatures.
	quartz	240	-66	-3.9		
	quartz	245	-63	-1.4		
Far Southeast	advanced argillic (vapor endmember)	550	-25	+7.0	1	• Its δD and $\delta^{18}O$ composition indicates late stage formation in a magmatic- hydrothermal system.
	advanced argillic	250	-28	+4.9	1	
	advanced argillic	250	-29	+2.5	1	
	advanced argillic	250	-38	+1.4	1	
	advanced argillic	250	-35	+2.8	1	
	advanced argillic	250	-38	+1.5	1	
	advanced argillic	250	-44	-0.6	1	
	advanced argillic	200	-44	-1.5	1	
	potassic (hypersaline endmember)	550	-45	+6.3	1	
sericitic (LLTL endmember)	350	-43	+5.7	1		
	sericitic	275	-51	+1.5	1	
Antamok	quartz	252	-79	-6.2	2	
	quartz	314	-72	-0.85	2	
Acupan	quartz	275	-76	-3.3	2	
Baguio-Mankayan	meteoric water		-68	-9.4	1, 2, 3	

- Its existence implies potential presence of undiscovered cogenetic porphyry Cu and high sulfidation epithermal mineralization in the underexplored southern part of the Mankayan Mineral District.

Southern Mankayan Mineral District



not to scale

